Inhomogeneous Magnetization Transfer (ihMT) imaging in the acute cuprizone mouse model of demyelination/remyelination

Andreea Hertanu, Lucas Soustelle, Julie Buron, Julie Le Priellec, Myriam Cayre, Arnaud Le Troter, Valentin H Prevost, Jean-Philippe Ranjeva, Gopal Varma, David C Alsop, et al.

NeuroImage 265 (2023) 119785

Contents lists available at ScienceDirect

NeuroImage

journal homepage: www.elsevier.com/locate/neuroimage

Inhomogeneous Magnetization Transfer (ihMT) imaging in the acute cuprizone mouse model of demyelination/remyelination

Andreea Hertanu[a,b], Lucas Soustelle[a,b], Julie Buron[a,b,c], Julie Le Priellec[c], Myriam Cayre[c], Arnaud Le Troter[a,b], Valentin H. Prevost[a,b], Jean-Philippe Ranjeva[a,b], Gopal Varma[d], David C. Alsop[d], Pascale Durbec[c], Olivier M. Girard[a,b], Guillaume Duhamel[a,b,*]

[a] Aix Marseille Univ, CNRS, CRMBM, Marseille, France
[b] APHM, Hôpital Universitaire Timone, CEMEREM, Marseille, France
[c] Aix Marseille Univ, CNRS, IBDM, Marseille, France
[d] Division of MR Research, Radiology, Beth Israel Deaconess Medical Center, Harvard Medical School, Boston, MA, United States

ARTICLE INFO

Keywords:
Myelin MR imaging
ihmt T_{1D}-filters
Demyelination
Remyelination
cuprizone mouse model
histology

ABSTRACT

Background: To investigate the association of ihMT (inhom signals with the demyelination and remyelination phases of the acute cuprizone mouse model in comparison with histology, and to assess the extent of tissue damage and repair from MRI data.

Methods: Acute demyelination by feeding 0.2% cuprizone for five weeks, followed by a four-week remyelination period was applied on genetically modified plp-GFP mice. Animals were scanned at different time points of the demyelination and remyelination phases of the cuprizone model using a multimodal MRI protocol, including ihMT T_{1D}-filters, MPF (Macromolecular Proton Fraction) and R_1 (longitudinal relaxation rate). For histology, plp-GFP (proteolipid protein – Green Fluorescent Protein) microscopy and LFB (Luxol Fast Blue) staining were employed as references for the myelin content. Comparison of MRI with histology was performed in the medial corpus callosum (mCC) and cerebral cortex (CTX) at two brain levels whereas ROI-wise and voxel-based analyses of the MRI metrics allowed investigating *in vivo* the spatial extent of myelin alterations.

Results: IhMT high-pass T_{1D}-filters, targeted toward long T_{1D} components, showed significant temporal variations in the mCC consistent with the effects induced by the cuprizone toxin. In addition, the corresponding signals correlated strongly and significantly with the myelin content assessed by GFP fluorescence and LFB staining over the demyelination and the remyelination phases. The signal of the band-pass T_{1D}-filter, which isolates short T_{1D} components, showed changes over time that were poorly correlated with histology, hence suggesting a sensitivity to pathological processes possibly not related to myelin. Although MPF was also highly correlated to histology, ihMT high-pass T_{1D}-filters showed better capability to characterize the spatial-temporal patterns during the demyelination and remyelination phases of the acute cuprizone model (e.g., rostro-caudal gradient of demyelination in the mCC previously described in the literature).

Conclusions: IhMT sequences selective for long T_{1D} components are specific and sensitive *in vivo* markers of demyelination and remyelination and have successfully captured the spatially heterogeneous pattern of the demyelination and remyelination mechanisms in the cuprizone model. Interestingly, differences in signal variations between the ihMT high-pass and band-pass T_{1D}-filter, suggest a sensitivity of the ihMT sequences targeted to short T_{1D}s to alterations other than those of myelin. Future studies will need to further address these differences by examining more closely the origin of the short T_{1D} components and the variation of each T_{1D} component in pathology.

1. Introduction

Inhomogeneous magnetization transfer (ihMT) MRI relies on the generation and decay of the dipolar order, a 'magnetization' order characteristic of tissues with motion-restricted molecules and unaveraged dipolar interactions (Varma et al., 2015). Hence the ihMT signal provides access to a new contrast weighted by the dipolar order relaxation time T_{1D} (Varma et al., 2017), a probe for tissue microstructure

* Corresponding author: Guillaume Duhamel. Centre de Résonance Magnétique Biologique et Médicale, Aix Marseille University, CNRS UMR 7339, 13005 Marseille, France, +33 491 386 260.
E-mail address: guillaume.duhamel@univ-amu.fr (G. Duhamel).

https://doi.org/10.1016/j.neuroimage.2022.119785.
Received 3 September 2022; Received in revised form 31 October 2022; Accepted 1 December 2022
Available online 1 December 2022.

and slow motional processes such as lipid membrane collective motions (Dufourc et al., 1992). In myelin, the alignment and mobility of the methylene protons along the lipid chains that make up the phospholipid bilayer structures are thought to be at the origin of the observed ihMT contrast (Varma et al., 2015; Manning et al., 2017).

In white matter (WM), where myelin accounts for around 50% of the total dry mass (Sanjeeva Reddy et al., 1983), T_{1D} has been initially reported to be in the order of a few milliseconds (Varma et al., 2017; Swanson et al., 2017; Prevost et al., 2017). However, a recent study performed with high power off-resonance RF pulses revealed that at least two T_{1D} components may contribute to the ihMT signal in myelinated tissues (Carvalho et al., 2020). A long T_{1D} component on the order of 10 ms and a short component around 500 μs were quantified in healthy WM structures (Carvalho et al., 2020). In line with the theory underlying ihMT (Varma et al., 2015; Manning et al., 2017), it was demonstrated that high saturation power is indeed necessary to reveal the signal associated with short T_{1D} components (Duhamel et al., 2019). Additionally, the ihMT signal can be weighted towards specific T_{1D} ranges by varying the switching time between RF pulses with opposite frequencies (Δt) (Prevost et al., 2017), a key parameter in the dual-frequency off-resonance saturation experiment of the ihMT sequence.

These ihMT contrast modulation mechanisms have been investigated and exploited recently to probe the signal contribution of specific T_{1D} components. A comprehensive theoretical and experimental analysis of the T_{1D}-weighting associated with ihMT was described and allowed the generation of high-pass and band-pass T_{1D}-filters dedicated to brain tissues (Hertanu et al., 2022a). Furthermore, a second study performed on healthy mice focused on the validation of the sensitivity and specificity to myelination of these T_{1D}-filters by comparing brain ihMT MRI data with histology (Hertanu et al., 2022b). Consistent with a dominant contribution of the long T_{1D} component in myelin, high specificity to healthy myelinated tissues was obtained for the high-pass T_{1D}-filter selective for the long T_{1D} component. In addition an increasing trend in specificity was noticed as the ihMT T_{1D}-filter was weighted towards longer T_{1D} ranges by Δt lengthening (Duhamel et al., 2019; Hertanu et al., 2022b). In contrast, for the band-pass T_{1D}-filter isolating short T_{1D} components in the 100 μs to 1 ms range, lower specificity and poor correlation with histology myelin biomarkers suggested a dominant contribution of non-myelin signal source (Hertanu et al., 2022b). Therefore, by providing access to different microstructural tissue components and features, ihMT might allow the evaluation of distinct biophysical mechanisms underlying myelin pathology.

To date, the potential of ihMT for myelin pathology has not been widely studied. IhMT was evaluated in clinical multiple sclerosis (MS) lesions, where it demonstrated higher correlations with the Expanded Disability Status Scale score as compared to the MT ratio (MTR) (Van Obberghen et al., 2018; Zhang et al., 2020). In a more recent study, ihMT was shown to be sensitive to non-compact myelin sheath in hypomyelinated white matter structures in the brain of shiverer mice, thus suggesting ihMT as a potential marker for myelin repair (Lee et al., 2022).

In the current study, we investigated the association between the ihMT signals obtained with various T_{1D}-filtering protocols and the demyelination and remyelination dynamics of the acute cuprizone mouse model (i.e., five weeks of continuous cuprizone diet followed by four weeks of recovery). The acute cuprizone model is mainly characterized by myelin related alterations, although infiltration of astrocytes, microglia and macrophages also accompanies the demyelination process (Skripuletz et al., 2011; Steelman et al., 2012; Hiremath et al., 1998) along with axonal damage (Stidworthy et al., 2006; Nyamoya et al., 2017; Höflich et al., 2016). The medial corpus callosum (mCC) was the primary focus of our analyses due to the extensive demyelination it presents and the consistency of the generated effect (Hiremath et al., 1998; Matsushima and Morell, 2001; Gudi et al., 2014; Vega-Riquer et al., 2019). IhMT signals were correlated with two histology biomarkers for myelin (proteolipid protein – Green Fluorescent Protein (plp-GFP) microscopy and Luxol Fast Blue (LFB) staining), and comparisons with the macromolecular proton fraction (MPF) and R_1, two MRI metrics which have previously demonstrated sensitivity to pathological-induced myelin alterations (Schmierer et al., 2004; Schmierer et al., 2007; Schmierer et al., 2008; Underhill et al., 2011; Thiessen et al., 2013; Janve et al., 2013; Turati et al., 2015; Hakkarainen et al., 2016; Khodanovich et al., 2017; Khodanovich et al., 2019; Soustelle et al., 2019) were performed. In a second step, taking advantage of the volumetric nature of the MRI datasets, ROI-based analyses along the rostro-caudal mCC and voxel-based analyses were carried out for ihMT, MPF and R_1 in order to identify the spatial extent and the significant signal variations over the time course of the acute cuprizone model.

2. Methods

2.1. Animal experiments

Animal studies were conducted in agreement with the French guidelines for animal care from the French Department of Agriculture (Animal Rights Division), the directive 2010/63/EU of the European Parliament and of the Council of 22 September 2010 and approved by our institutional committee on ethics in animal research (Comité d'Ethique de Marseille n°14, project authorization APAFIS#1747–2015062215062372v6).

A total of twenty-two genetically modified plp-GFP mice of the C57BL/6 strain were included in this study. The GFP is specifically expressed in myelinating oligodendrocytes and the GFP fluorescence is a direct measurement of the expression of the PLP protein, the major protein constituting myelin. Thus, the plp-GFP transgenic mice represent a valuable and direct tool for the quantification of the myelin content by circumventing some of the drawbacks of protein antibody techniques, such as staining saturation or inhomogeneous stain penetration which might induce nonlinear scaling between the staining intensity and the myelin content.

Demyelination was induced for all mice at once by cuprizone administration in standard chow (0.2% w/w) for five weeks. The spontaneous remyelination which takes place after the termination of the cuprizone diet was followed for four weeks. Specifically, mice were divided into two groups: a longitudinal group ($N = 4$ mice) followed-up over nine weeks, and a time point group ($N = 18$ mice). The four mice in the longitudinal group underwent only MRI scans at all the defined time points: Week 0 (W_0), Week 3 (W_3), Week 5 (W_5), Week 7 (W_7), and Week 9 (W_9). Their role was to increase the statistical power of the voxel-wise analyses on the MRI metrics. The mice in the time point group underwent only one MRI session at one defined time point prior to sacrifice and histological analyses. Fig. 1 illustrates the experimental design and the distribution of mice in each group at the investigated time points of the demyelination ($W_0 \rightarrow W_5$) and remyelination ($W_5 \rightarrow W_9$) phases.

2.2. Data acquisition

2.2.1. MRI metrics

In vivo MRI experiments were performed on a preclinical 7T scanner (PharmaScan; Bruker), using a 72-mm body volume coil and a four-channel phased array receive-only MRI CryoProbe (Bruker) for RF transmission and RF reception, respectively. During scans under isoflurane anesthesia (1.5%, constant flow, 300 mL/min; Univentor 400 anesthesia unit, Univentor), animal respiratory rate and temperature were monitored using a small animal respiratory pillow and a fiber optic rectal probe respectively (Model 1030, MR-compatible ERT Monitoring & Gating System, SA Instruments). Respiration was maintained at 100 ± 10 breaths/min using minor adjustments to the isoflurane concentration. Body temperature was maintained at 37.5 ± 0.5 °C using a heating blanket connected to a water bath system.

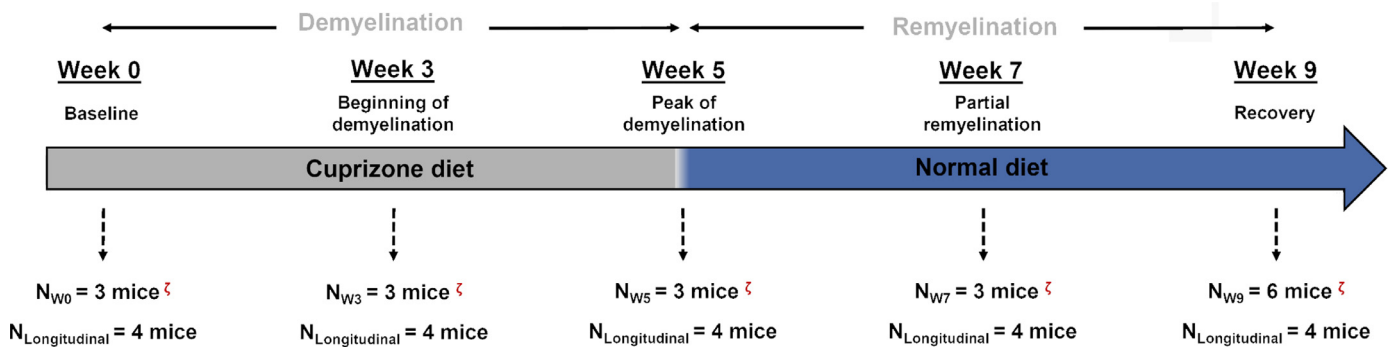

Fig. 1. Experimental design for the investigation of the cuprizone-induced demyelination and remyelination phases. For the time point group, N_{Wi} ($i = \{0; 3; 5; 7; 9\}$), mice were scanned only once before histological analyses (indicated by the "ζ" symbol). The 4 mice in the longitudinal group, $N_{Longitudinal}$, were scanned at all time points.

Table 1
Saturation and readout parameters of the ihMTRAGE and MT-, VFA- and AFI-SPGR sequences. For ihMTRAGE, a low-duty cycle (DC) saturation scheme was achieved by using N_{bursts} bursts of N_p pulses, repeated every BTR. The duration of the pulses (pw) is indicated, as well as the offset saturation frequency (Δf), the switching time (Δt), the corresponding root-mean-square (B_{1RMS}) and peak power (B_{1peak}). For VFA-SPGR, the various flip angle (α) values are reported, and for the AFI-SPGR sequence, the echo time (TE) and the two repetition times (TR_1 and TR_2). The different values of acquisition times (TA) for the ihMTRAGE sequence relate to the different number of repetitions (NEX) associated to the various switching times (Δt).

Sequence	ihMTRAGE	MT-SPGR	VFA-SPGR	AFI-SPGR
Saturation parameters	• pw = 0.5 ms • Δt = 0.0[(a)], 0.8[(b)], 3.2[(c)] ms • Δf = 10 kHz • B_{1RMS} = 6.7 μT • B_{1peak} = 42.4 μT • N_p = 8 • N_{bursts} = 15 • BTR = 60 ms • DC = 6.67%	• pw = 10.25 ms • Δf = 6 kHz • B_{1RMS} = 5.0 μT • B_{1peak} = 9.1 μT	–	–
Readout parameters	• TE = 2.1 ms • TR = 2500.0 ms • NEX = 6[(a)]/12[(b)]/18[(c)] • Matrix size: 192x192x8 • Voxel size: 100x100x750 μm^3	• TE = 2.2 ms • TR = 30.0 ms • NEX=1 • Matrix size: 192x192x64 Voxel size: 100x100x750 μm^3	• α = 6°/10°/25° • TE = 2.2 ms TR = 30.0 ms • NEX=1 • Matrix size: 192x192x64 Voxel size: 100x100x750 μm^3	• TE = 2 ms • TR_1 = 15 ms • TR_2 = 60 ms • NEX=1 • Matrix size: 48x48x44 • Voxel size: 400x400x750 μm^3
Acquisition time	• TA = 8 min 40 s[(a)] 11 min 20 s[(b)] 22 min[(c)]	• TA = 4 min 32 s	• TA = 9 min 30 s	• TA = 1 min 59 s

T_2-weighted (T_2w) anatomical images were acquired along with specific sequences for the generation of the semi-quantitative and quantitative metrics of interest to assess myelination: ihMTsat, MPF and R_1. The protocols have been thoroughly described in previous work (Hertanu et al., 2022b). In brief, a slab-selective 3D low duty cycle (Varma et al., 2018; Mchinda et al., 2018) ihMT rapid gradient echo (ihMTRAGE) (Varma et al., 2020) sequence was used with various values of the dual-frequency offset switching time (Δt) (see Fig. 1, reference (Hertanu et al., 2022a)) such that ihMT high-pass and band-pass T_{1D}-filters could be generated from the acquired data. The saturation parameters previously optimized for the generation of ihMT high-pass and band-pass T_{1D}-filters that isolate the long and short T_{1D} components in the mouse brain (Hertanu et al., 2022a) are reported in Table 1. MTw-SPGR (Spoiled Gradient Recalled Echo), VFA-SPGR (Variable Flip Angle) and AFI-SPGR (Actual Flip Angle) sequences with optimized parameters for the single-point MPF strategy (Soustelle et al., 2020) (Table 1) were acquired and processed to derive MPF and R_1 maps. The B_1^+ map resulted from the AFI-SPGR acquisition and the R_1 map were also employed for the calculation of the ihMTsat metric (Munsch et al., 2021). A diagram summarizing the acquisition and the processing steps from the raw images to the final quantitative metrics is provided in Fig. 1 of reference (Hertanu et al., 2022b). MR acquisitions covered the brain volume in which the corpus callosum was present.

2.2.2. Histology metrics

For histology analyses, mice of the time point group were sacrificed (ketamine 150 mg/kg with xylazine 15 mg/kg) and intracardially perfused with phosphate-buffered saline and a 4% paraformaldehyde fixative solution. Mouse brains were extracted, post-fixed for 2 h in 4% paraformaldehyde and cryopreserved overnight in 20% sucrose. Frozen brains were sectioned into 20-μm thick histological slices (Cryostat Leica CM305S) in the rostro-caudal direction at 2 different brain locations with respect to bregma (bregma + 0.7 mm, referenced hereafter as anterior, and bregma – 1.0 mm, referenced hereafter as posterior). The identification of the two brain locations was accomplished by using the Allen mouse brain atlas (atlas.brain-map.org) as a reference.

Images with the green fluorescent protein (GFP) biomarker were acquired using a Zeiss fluorescence microscope with a 5x objective and a fixed exposure time. For the LFB analyses, brain slices were further prepared by post-fixation in methanol for 2 min at -20 °C, then rinsed in ethanol/acetic acid during 3 h at 60 °C. After rinsing in ethanol 96%, sections were decolorized in lithium carbonate 0.05% for 1 min and rinsed in ethanol 70%. Sections were then dehydrated through in-

creasing ethanol gradients (from 70% to 100%) and mounted in Eukitt (VWR). Images were acquired using a Zeiss AxioImager microscope with a 5x objective.

2.3. MRI post-processing

The derivation of the MRI metrics was accomplished following the same procedure thoroughly described in previous work (see Fig. 1 in reference (Hertanu et al., 2022b)). Briefly, ihMTsat (i.e., an ihMT metric unbiased for B_1^+/T_1 effects) (Hertanu et al., 2022b; Munsch et al., 2021; Rowley et al., 2021) was calculated from MT-weighted images acquired with single-frequency and dual-frequency off-resonance saturation using a home-built pipeline available at https://github.com/lsoustelle/SP_qMT_proc (hash f3f49e0). Increasing switching time values (Δt = 0.0; 0.8; 3.2 ms) used for the dual offset saturation led to the derivation of ihMT high-pass T_{1D}-filters with increasing T_{1D}-cutoff values (Hertanu et al., 2022a). Note that Δt of 0.0 ms (simultaneous dual frequency offset saturation) was obtained by cosine-modulating the RF saturation pulses. In addition a band-pass T_{1D}-filter was generated from the difference of ihMTsat images obtained with $\Delta t_{0.0}$ and $\Delta t_{0.8}$ as described in (Hertanu et al., 2022a). The macromolecular proton fraction (MPF) metric was derived from the binary spin-bath model for MT (Yarnykh, 2002; Yarnykh, 2012; Yarnykh et al., 2020), using the single-point measurement strategy with optimally constrained parameters (Soustelle et al., 2020). The longitudinal relaxation rate R_1 was estimated using the Ernst equation (Chang et al., 2008) applied to the VFA dataset. MPF and R_1 were both corrected for B_1^+ inhomogeneities (Yarnykh et al., 2020) estimated from the AFI dataset using a home-built pipeline available at https://github.com/lsoustelle/SP_qMT_proc (hash 05f43a4).

Following the pipeline presented in (Hertanu et al., 2022a) for the MRI volumes, native T_2w images acquired on all mice were employed to generate a T_2w template built in the same reference as the T_2w Dorr template with an isotropic resolution of 80x80x80 μm^3 (Dorr et al., 2008) by means of iterative non-linear transformations using the Advanced Normalization Tools (ANTs; v2.0.1) (Avants et al., 2009). The mouse-wise estimated transformations were applied on all the acquired images. Thus, by averaging the resulting images over all mice, templates were obtained for each MRI metric in the same reference space as that of the T_2w template.

2.4. Quantifications and analyses

Fig. 2 includes an example of anterior and posterior T_2w images and GFP images obtained at + 0.7 mm and – 1.0 mm from bregma respectively. An illustration of a sagittal view of the mouse brain extracted from (Paxinos and Franklin, 2019) and a landmark (gray vertical line) indicate the location of anterior and posterior slices. Examples of ROIs in mCC and the cerebral cortex (CTX) are also shown in blue and red, respectively.

2.4.1. Quantification of MRI metrics

The masks of the mCC and the CTX from the Dorr atlas were propagated onto the in-house built templates. Then, masks were propagated onto the native MRI images of each mouse by applying the inverse transformation estimated from the registration of the native individual images of each mouse onto their corresponding template. Masks were manually checked and corrected for imperfections in order to ensure the agreement with the histology manually segmented ROIs.

Quantifications of the MRI metrics were done native image-wise or template-wise depending on the performed analysis. First, the slice corresponding to the bregma level was identified with the help of the Allen mouse brain atlas on both the template and the individual native images. The remaining slices were then attributed to rostral and caudal brain locations. For the individual native image-based quantifications, the anterior slice (bregma + 0.7 mm) and posterior slice (bregma – 1.0 mm) were considered for comparisons with similar locations analyzed by histology (Fig. 2). Results obtained in the mCC at the rostral or anterior level are reported as mCC_{ANT}, and results obtained in the mCC at the caudal or posterior level are reported as mCC_{POST}. Due to their similar values, results obtained in the CTX at the anterior and posterior levels were averaged and reported as a single value. For the template-based quantifications, each slice from bregma + 1.20 mm to bregma – 2.16 mm was considered, leading to a total of forty-three slices.

2.4.2. Histology quantification

CTX, mCC_{ANT} and mCC_{POST} ROIs were manually drawn on the GFP and LFB histology images (Fig. 2) by two expert observers (J.L.P. and M.C.) by using the Allen mouse brain atlas as a reference. Plp-GFP fluorescence and LFB optical density were quantified in ImageJ (National Institute of Health) employing the procedure described in (Hertanu et al., 2022b). The mean and standard deviation values corrected for the background noise measured in the ventricles were calculated for each ROI.

2.4.3. Comparison of MRI metrics with histology metrics

The individual native MRI images of mice in the time point groups were considered for the comparison with histology. Mean values were quantified in mCC_{ANT}, mCC_{POST} and CTX regions of interest for each mouse. Due to experimental acquisition issues (motion and respiratory instabilities during the acquisition protocol), one mouse at W_0 and one mouse at W_5 had to be discarded from the analysis.

The normality of the data was assessed in JMP (v.16.0.0; SAS Institute) using the Shapiro-Wilk test. The homogeneity of variance was examined using Bartlett's test. A one-way analysis of variance (ANOVA) for each phase of the study (demyelination and remyelination) was followed by post-hoc Tukey's HSD two-by-two tests to determine significant differences in the signal dynamics of all MRI and histology metrics for the three abovementioned ROIs. Pearson's correlations were performed between MRI metrics and the LFB and GFP signals for the demyelination phase, the remyelination phase, as well as for the entire temporal dynamics (demyelination + remyelination). Statistical significance was defined as a *p-value* below the 0.05 threshold.

Pairs of significant correlation coefficients were tested for differences using the Steiger's modification of Dunn and Clark's z approach (Steiger, 1980) and the Zou's confidence interval (Zou, 2007) from the cocor package (Diedenhofen and Musch, 2015) for overlapping correlations based on dependent groups in R (v.1.4.1106; RStudio, PBC) in order to determine to which histology reference the MRI metrics correlated best.

2.4.4. Spatial-temporal profiles of the cuprizone model along the mCC assessed by MRI

The template-based quantifications for the mice in the longitudinal and the time point groups were considered in this analysis. The spatial-temporal profiles of signal variation in the mCC along the rostral-caudal direction were calculated for each MR metric as follows: the mean values of the different MRI metrics were measured at all time points in mCC ROIs across the 43 brain slices covering the entire callosal structure. The percentage of variation relative to baseline (W_0) was calculated for each metric and each slice as:

$$\delta\mathrm{Metric}_{W_i} = 100 \times \frac{\mathrm{Metric}_{W_i} - \mathrm{Metric}_{W_0}}{\mathrm{Metric}_{W_0}}$$

Where $i = \{3;5;7;9\}$. The $\delta\mathrm{Metric}_{W_i}$ values were then plotted as a function of the slice location with smoothing using a gaussian sliding window with σ=5 voxels under Matlab (R2017b, MathWorks Inc.).

2.4.5. Voxel-wise analyses

The individual native images of mice in the longitudinal and time point groups co-registered in the template space were used to perform a voxel-based morphometry (VBM) analysis. The number of mice employed for each time point was 6, 7, 6, 7 and 10 for W_0, W_3, W_5, W_7

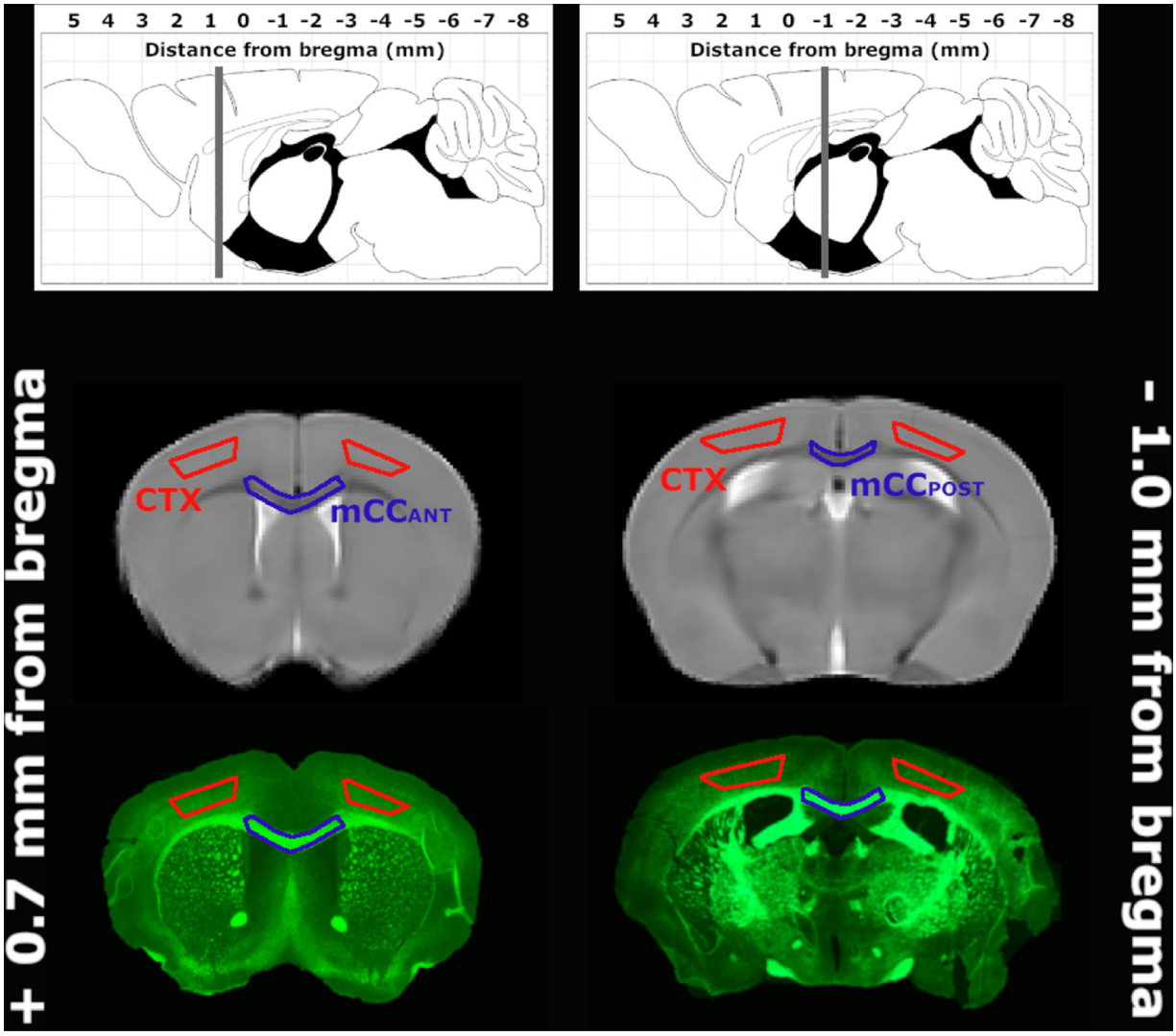

Fig. 2. Sagittal view of the mouse brain indicating the position with respect to the bregma for the rostral or anterior (+ 0.7 mm from bregma) and caudal or posterior (– 1.0 mm from bregma) brain slices investigated by both MRI and histology analyses. Sagittal images were adapted from ((Paxinos and Franklin, 2019)). Template T_2w and GFP axial images are illustrated. Examples of ROIs taken in the anterior and posterior medial corpus callosum (mCC_{ANT} and mCC_{POST}, respectively) and the cerebral cortex (CTX) are depicted in blue and red, respectively. (For interpretation of the references to colour in this figure legend, the reader is referred to the web version of this article.)

and W_9, respectively. The objective was to localize the extent of voxels exhibiting a significant signal variation during the demyelination (W_0-W_3-W_5) and remyelination (W_5-W_7-W_9) phases in the acquired brain volume covered by the MRI acquisitions.

First, the general linear model routine from the FMRIB software library (FSL v.6.0.3) was used to generate the design matrix for a one-factor and three-levels ANOVA analysis. The factor represents each MRI metric in turn and the three-levels represent the three time points characterizing the demyelination (W_0-W_3-W_5) and remyelination (W_5-W_7-W_9) phases. The design matrices were used as inputs in the randomize routine from the same software using a threshold-free cluster enhancement option (Winkler et al., 2014) and 10,000 permutations (Wakana et al., 2007). From the family-wise error corrected (1 – *p-value*) maps, a binary mask was generated by thresholding all *p-values* below 0.01. The mask was afterwards applied on the F-contrast maps to obtain the significant F-statistics values.

The AimsMesh function from the BrainVISA software (Rivière et al., 2003) (v.5.0.4, IFR49) was used with a smoothing option of 500 iterations in order to generate meshes from the slice-wise binary masks of the brain and of the corpus callosum. The significant F-maps were binarized and the same approach was used to generate the corresponding meshes. The Anatomist interface from BrainVISA was used to visualize all the resulting renderings, which were overlapped in order to obtain the 3D localization of significant clusters in the brain.

3. Results

3.1. Demyelination and remyelination dynamics in the cuprizone model: comparison between MRI and histology

3.1.1. Temporal dynamics and correlation analyses in mCC_{ANT} and mCC_{POST}

The expected demyelination and remyelination phases in the cuprizone model were well captured by the various MRI metrics as demonstrated visually in Fig. 3 and Fig. 4. IhMT T_{1D}-filters, MPF and R_1 maps at anterior and posterior levels are illustrated at remarkable time points, including W_0 (baseline), W_5 (peak of demyelination) and W_9 (maximum recovery). Images at the intermediate time points (W_3 and W_7) are provided in Appendix A (Fig. A1 and Fig. A2). During demyelination, the most important signal loss in the caudal brain (posterior level, bregma

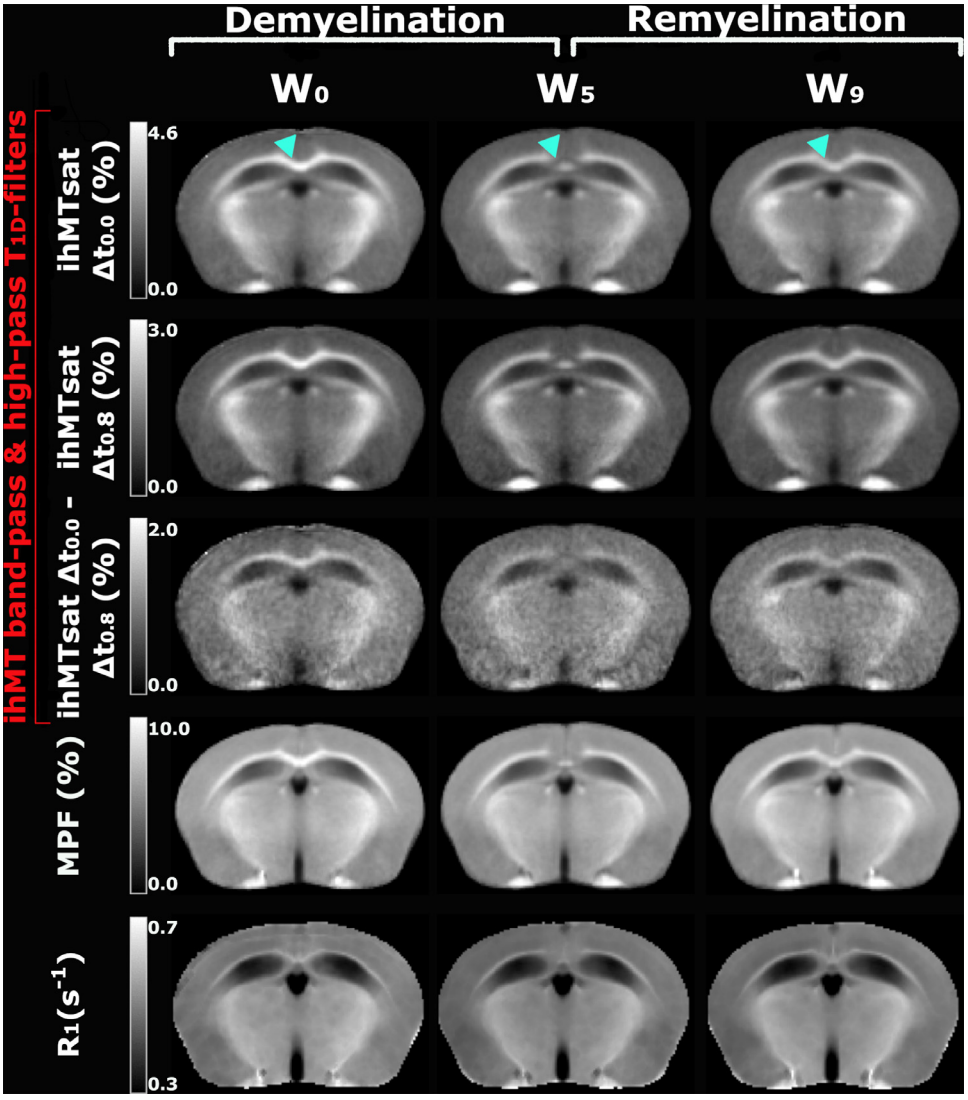

Fig. 3. Representative template-based posterior images (at – 1.0 mm from the bregma level) for ihMT high-pass and band-pass T_{1D}-filters, MPF and R_1. The signal range for each metric is indicated in its absolute units. The time points of the study illustrated are: W_0 – baseline: maximum signal intensity in all structures, W_5 – peak of demyelination with a maximum signal loss in the mCC_{POST} (indicated by the cyan arrowheads) accompanied by a signal preservation in the dorsal fornix and W_9 – remyelination with a perceived incomplete signal recovery.

– 1.0 mm) was observed in the mCC for all MRI metrics as pointed out by the cyan arrows in Fig. 3. At W_5, the dorsal fornix, a white matter bundle localized in the mesial part of the cerebral hemispheres, appears to be spared from intensive demyelination as highlighted by the substantial remaining signal. Rostrally (anterior level, bregma + 0.7 mm), the signal loss was more pronounced in the lateral CC as compared to the mCC (green arrows in Fig. 4).

During remyelination, a recovery of signal for all metrics is observed, although remaining incomplete at W_9 compared to W_0. This is particularly evident in the mCC. An illustrative qualitative comparison with histology is visible in Fig. 5, which depicts the magnified ihMTsat $\Delta t_{0.8}$ images along with LFB and GFP histology images with a focus on the mCC at the posterior level (mCC_{POST}; upper rows) and at the anterior level (mCC_{ANT}; lower rows). The magenta arrows in Fig. 5 outline the preserved dorsal fornix for both MR and histology metrics at W_5.

A quantitative characterization of the demyelination and remyelination phases in the cuprizone model for mCC_{ANT} and mCC_{POST} is provided in Fig. 6, which shows the temporal evolution of the mean absolute value calculated over the mice in the time point group for each one of the investigated metrics. Radar plots of Fig. 7 present for each metric the relative variation with respect to the baseline (mean absolute value at each time point normalized by the mean absolute value at W_0). This normalization emphasizes differences in the quantity of signal loss or signal gain between the various metrics in the mCC at the anterior and posterior levels and allows a direct visual comparison of all metrics.

Data points respected the assumptions of normality and homogeneity of variance. Significant differences between the signal at various time points for each metric as revealed by the ANOVA and the post-hoc tests are summarized in Table 2.

During demyelination, the temporal dynamics of MRI metrics in both the mCC_{ANT} and mCC_{POST} demonstrated a closer resemblance to that of GFP than of LFB. Indeed, while GFP and the MRI metrics show the highest percentage of signal loss between W_0 and W_3, LFB signal loss appears to be greatest between W_3 and W_5 (Fig. 7a and Fig. 7b). Statistical tests indicate nonetheless a significant signal variation between all the time points during the demyelination phase for the histology metrics, except between W_0 and W_3 in mCC_{ANT}. IhMT T_{1D}-filters and MPF (Table 2) show fewer significant differences. This is particularly evidenced for MPF in the mCC_{ANT} and for the ihMT band-pass T_{1D}-filter. Finally, no significant differences were found for R_1.

Concerning the percentage of signal loss at the demyelination peak (W_5) in mCC_{POST}, ihMT signals for which the contribution of short T_{1D} components is highly attenuated (ihMTsat $\Delta t_{3.2}$, ihMTsat $\Delta t_{.0.8}$) presented a signal loss down to 58%, thus approaching most the percentage of signal loss obtained for GFP (i.e., 47%). Signals presenting a contribution from the short T_{1D} components (ihMTsat $\Delta t_{0.0}$, ihMTsat $\Delta t_{0.0}$ - ihMTsat $\Delta t_{0.8}$ and MPF) show only a moderate loss, with signals at W_5 being 61%, 65% and 71% of signals at W_0 respectively. For R_1, the signal loss at W_5 was the lowest, down to only 90% as compared to W_0. A similar behavior was observed in mCC_{ANT}. The magnitude of the signal

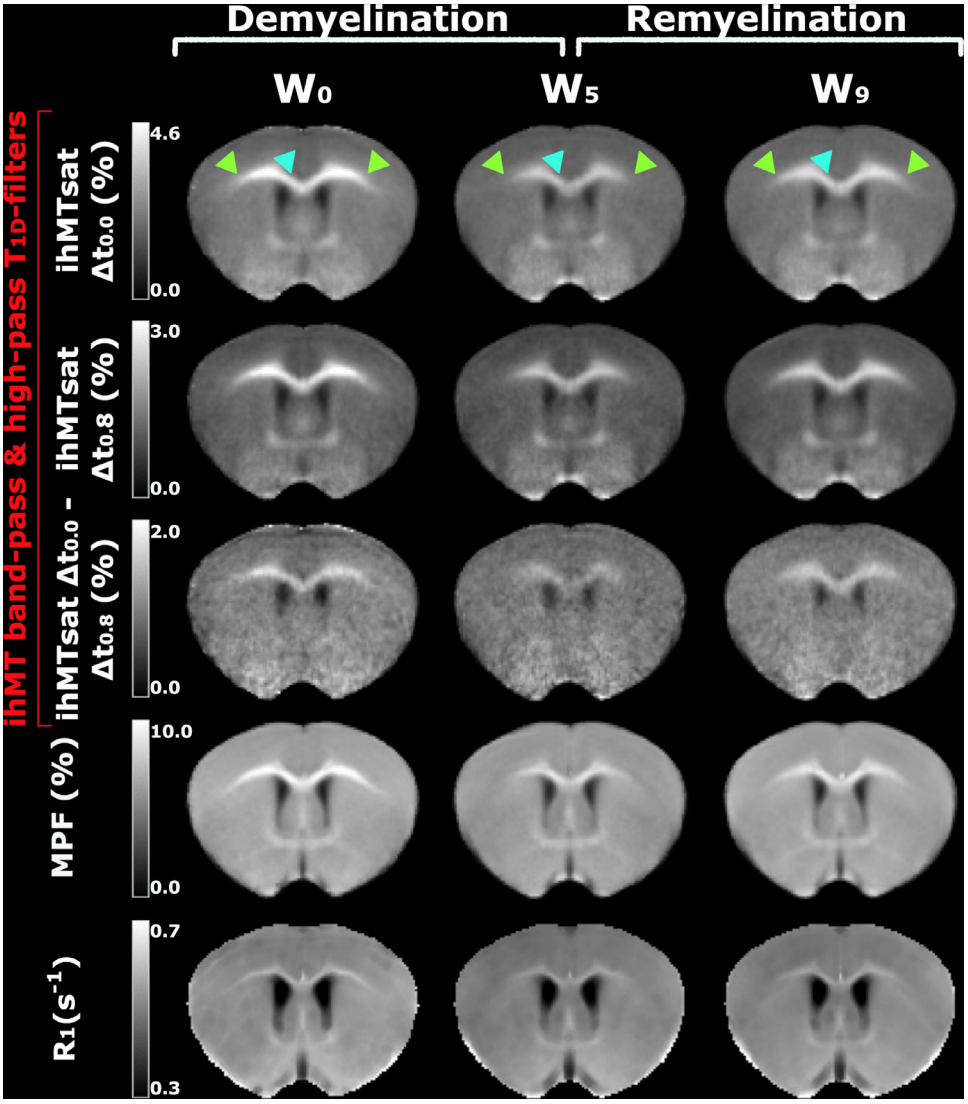

Fig. 4. Representative template-based anterior images (at + 0.7 mm from the bregma level) for ihMT high-pass and band-pass T_{1D}-filters, MPF and R_1. The signal range for each metric is indicated in its absolute units. The time points of the study illustrated are: W_0 – baseline: maximum signal intensity in all structures, W_5 – peak of demyelination with a signal loss in the mCCANT (cyan arrowheads) and an even stronger signal loss in the lateral part of the CC (green arrowheads) and W_9 – remyelination with a perceived incomplete signal recovery in both mCC_{ANT} and the lateral CC. (For interpretation of the references to colour in this figure legend, the reader is referred to the web version of this article.)

Table 2
Results of the ANOVA tests for the demyelination (W_0-W_3-W_5) and the remyelination (W_5-W_7-W_9) phases, followed by post-hoc Tukey HSD two-by-two comparisons in the mCC_{ANT} and mCC_{POST}. If the differences are statistically significant (*p-value* < 0.05) then mCC_{ANT} and mCC_{POST} are indicated in the table. In the contrary case, *p-value* > 0.05 is reported. The difference between the basal (W_0) and final (W_9) signal intensities were tested by employing a *t*-test. *P-values* below the threshold 0.05 were considered significant.

Statistical tests		ihMTsat $\Delta t_{0.0}$	ihMTsat $\Delta t_{0.8}$	ihMTsat $\Delta t_{3.2}$	ihMTsat $\Delta t_{0.0}$ - $\Delta t_{0.8}$	MPF	R_1	GFP	LFB
Demyelination	**ANOVA (W_0-W_3-W_5)**	**mCC_{ANT} mCC_{POST}**	**mCC_{ANT} mCC_{POST}**	**mCC_{ANT} mCC_{POST}**	**mCC_{ANT} mCC_{POST}**	**mCC_{POST}**	***p-value* > 0.05**	**mCC_{ANT} mCC_{POST}**	**mCC_{ANT} mCC_{POST}**
	W_0-W_3	**mCC_{ANT} mCC_P**	**mCC_{ANT} mCC_{POST}**	**mCC_{ANT} mCC_{POST}**	**mCC_{ANT}**	**mCC_{POST}**	***p-value* > 0.05**	**mCC_{POST}**	**mCC_{POST}**
	W_0-W_5	**mCC_{ANT} mCC_{POST}**	**mCC_{ANT} mCC_{POST}**	**mCC_{ANT} mCC_{POST}**	**mCC_{ANT} mCC_{POST}**	**mCC_{POST}**	***p-value* > 0.05**	**mCC_{ANT} mCC_{POST}**	**mCC_{ANT} mCC_{POST}**
	W_3-W_5	**mCC_{POST}**	**mCC_{POST}**	***p-value* > 0.05**	***p-value* > 0.05**	***p-value* > 0.05**	***p-value* > 0.05**	**mCC_{ANT} mCC_{POST}**	**mCC_{ANT} mCC_{POST}**
Remyelination	**ANOVA (W_5-W_7-W_9)**	**mCC_{POST}**	**mCC_{POST}**	**mCC_{POST}**	**mCC_{POST}**	**mCC_{POST}**	**mCC_{POST}**	**mCC_{ANT} mCC_{POST}**	**mCC_{ANT} mCC_{POST}**
	W_5-W_7	**mCC_{POST}**	**mCC_{POST}**	**mCC_{POST}**	***p-value* > 0.05**	**mCC_{POST}**	***p-value* > 0.05**	**mCC_{ANT} mCC_{POST}**	**mCC_{ANT} mCC_{POST}**
	W_5-W_9	**mCC_{POST}**	**mCC_{POST}**	**mCC_{POST}**	**mCC_{POST}**	**mCC_{POST}**	**mCC_{POST}**	**mCC_{ANT} mCC_{POST}**	**mCC_{ANT} mCC_{POST}**
	W_7-W_9	***p-value* > 0.05**							
Basal vs. final	**W_0-W_9**	**mCC_{ANT} mCC_{POST}**	**mCC_{ANT} mCC_{POST}**	**mCC_{POST}**	***p-value* > 0.05**	**mCC_{ANT} mCC_{POST}**	**mCC_{ANT}**	***p-value* > 0.05**	**mCC_{POST}**

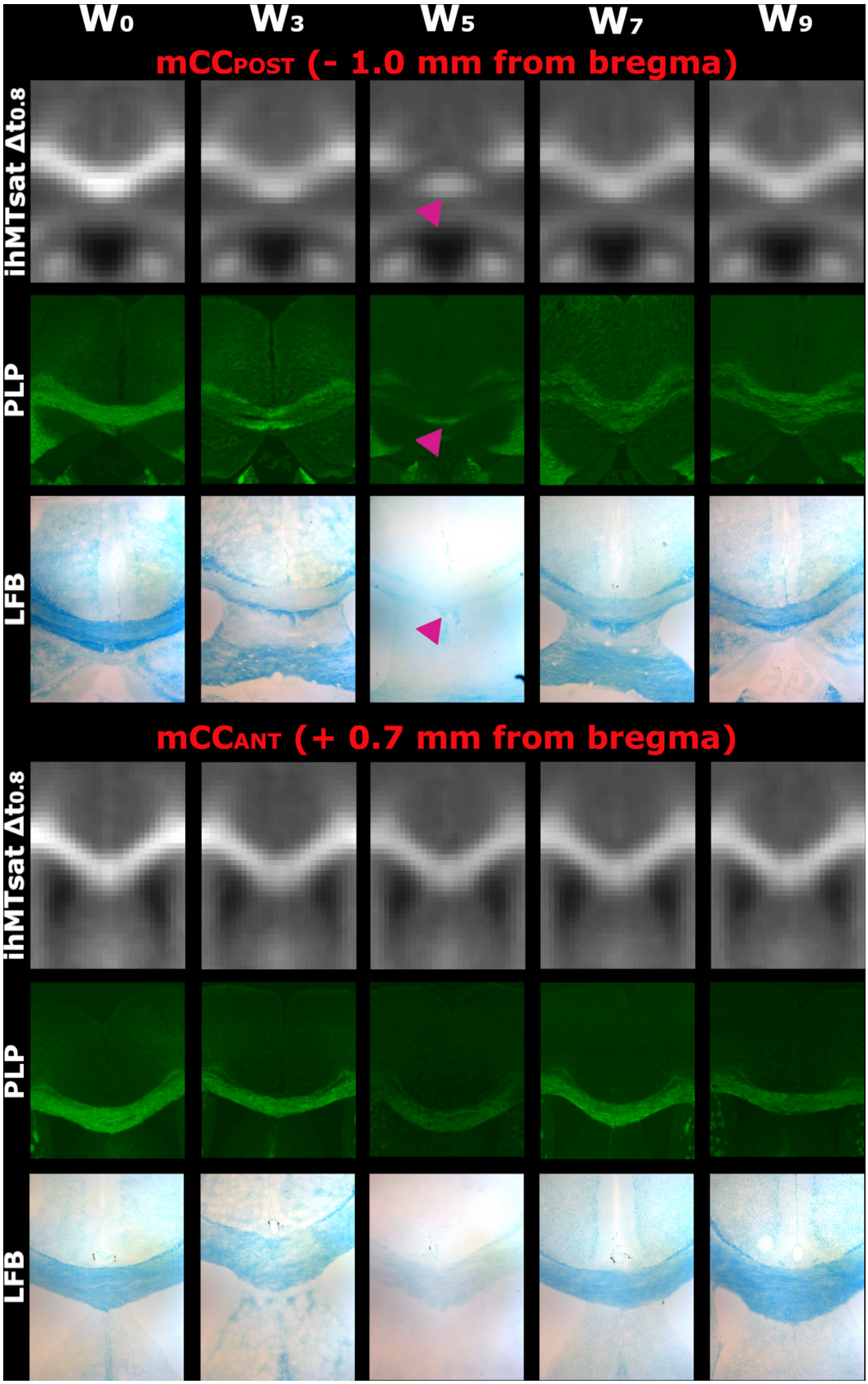

Fig. 5. Insets on the medial corpus callosum for ihMTsat $\Delta t_{0.8}$ (represented in Fig. 3 and Fig. 4) and plp-GFP and LFB histology metrics. In contrast with the mCC_{POST}, the dorsal fornix (magenta arrowheads) does not undergo extensive demyelination as highlighted by the preserved signal of all metrics.

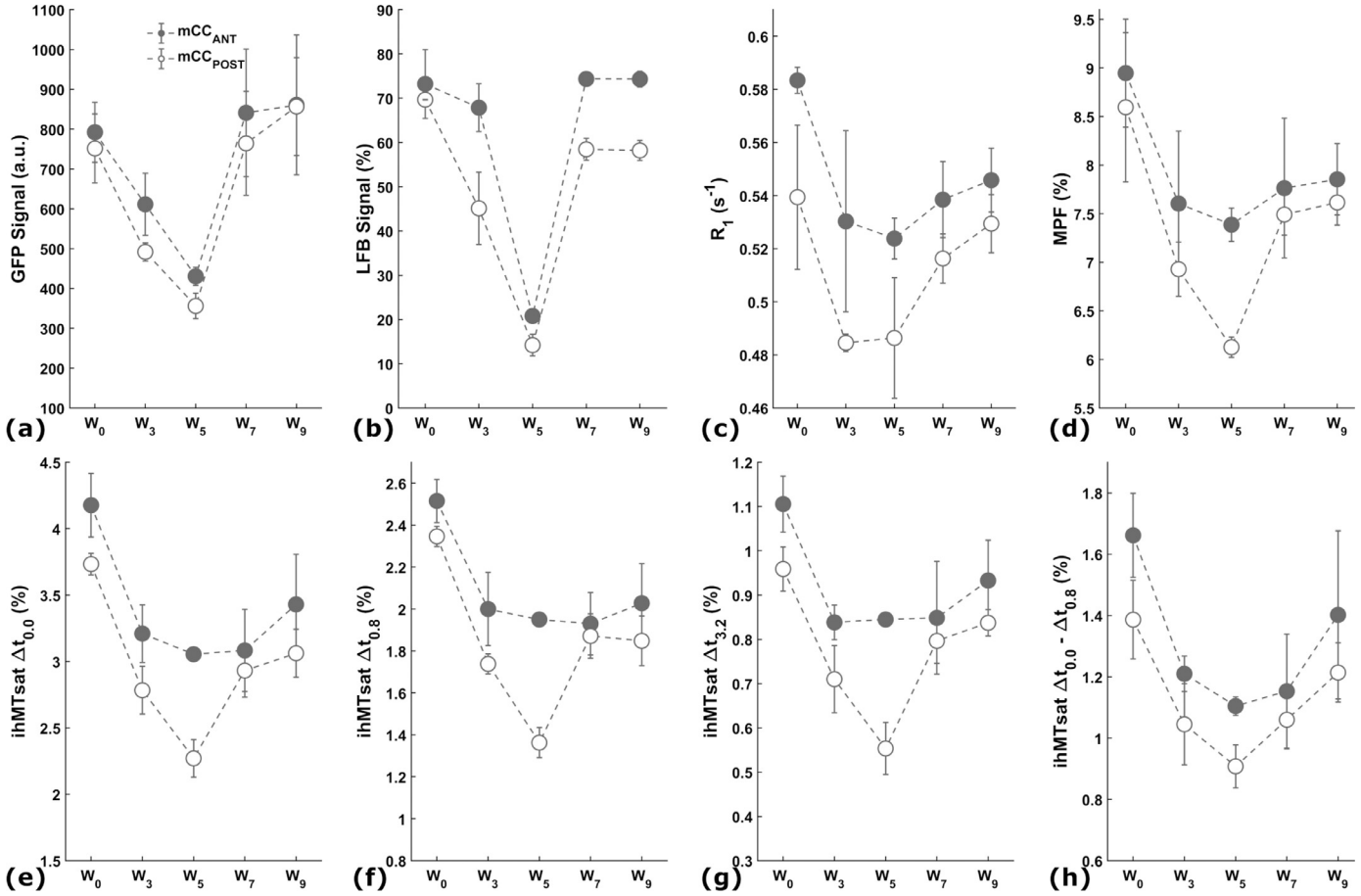

Fig. 6. Evolution in absolute units of all the investigated metrics in mCC_{ANT} and mCC_{POST} during the demyelination and remyelination phases of the cuprizone model: (a) GFP, (b) LFB, (c) R_1, (d) MPF, (e-g) ihMT high-pass T_{1D}-filters and (h) ihMT band-pass T_{1D}-filter. The mean value and standard deviation were calculated over the mice in the time point group at each week. During the demyelination phase (W_0 to W_5), the acute intoxication resulted in a loss of signal for all metrics, notably higher in mCC_{POST} as compared to mCC_{ANT}. Remyelination (W_5 to W_9) resulted in the expected reversal in trends, although recovery of signal was only partial for MR metrics. The scale of Y-axes was adjusted for each metric in order to better appreciate of the signal variations.

loss for all metrics was, however, far weaker (Fig. 7b). Thus, the signal was reduced to 54% for GFP, on the order of 66–78% for the various ihMT T_{1D}-filters and greater than 80% for MPF and R_1.

During remyelination in the mCC_{POST}, the dynamics of ihMT high-pass T_{1D}-filters and MPF show the highest and statistically significant increase between W_5 and W_7 (Table 2), thereby following that of histology (Fig. 7c). Conversely, differences in the band-pass T_{1D}-filter and R_1 metrics between W_5 and W_7 were not significant (Table 2). Between W_7 and W_9 none of the differences in MRI metrics were found significant (Table 2). The signal variation of MRI metrics accompanying the remyelination in the mCC_{ANT} (Fig. 7d) was less consistent with histology. Another important difference between MRI metrics and histology is a trend for an incomplete recovery of MRI metrics. This is illustrated in Fig. 6, Fig. 7c and Fig. 7d where the points corresponding to W_9 are lower than the points at W_0 (*p-value* < 0.05 for ihMT high-pass T_{1D}-filters and MPF in mCC_{POST} and mCC_{ANT}, except for the $\Delta t_{3.2}$ in mCC_{ANT}).

In terms of correlation analyses between the MRI and histology metrics (Table 3), Pearson's correlation coefficients were overall higher for mCC_{POST} as compared to mCC_{ANT}. Additionally, correlations in mCC_{ANT} were not significant when MRI metrics were associated with LFB during the demyelination phase and no significant correlations were found during the remyelination phase. In mCC_{POST}, for both the demyelination and remyelination phases, highest statistically significant correlation coefficients with GFP and LFB were found for the ihMT high-pass T_{1D}-filters and MPF. When the entire temporal dynamics was considered, no significant correlations were found for mCC_{ANT}, while for mCC_{POST} all MRI metrics presented statistically significant correlation coefficients when compared to LFB. When compared to GFP only ihMTsat $\Delta t_{3.2}$, MPF and R_1 showed significant correlations. Additionally, correlation analyses over the entire dynamics led to overall lower correlation coefficients as compared to the phase-wise analyses. Regression analyses are shown in Fig. 8 and Fig. 9 for mCC_{POST} and mCC_{ANT}, respectively.

3.1.2. *Comparisons between correlation coefficients*

When comparing the significant correlation coefficients obtained in mCC_{POST} for associations between the ihMT high-pass T_{1D}-filters and MPF with each of the two histology references (Table 4, Fig. 8), no statistically significant differences were found during demyelination (*p-value* > 0.05). The same analysis during remyelination yields significantly higher correlation coefficients with LFB for ihMTsat $\Delta t_{0.0}$, ihMTsat $\Delta t_{0.8}$ and MPF (*p-value* < 0.05). The non-significant difference obtained for ihMTsat $\Delta t_{3.2}$ (*p-value* = 0.12) is potentially due to the lower SNR of this T_{1D}-filter.

3.2. *Spatial-temporal profiles of the cuprizone model along the mCC*

The spatial-temporal profiles of signal loss for the MRI metrics ($\delta Metric_{Wi}$) measured in the mCC are shown in Fig. 10. A clear distinction is present for most of the MRI metrics between their profiles in the rostral (> 0.0 mm from bregma) and the caudal part (< 0.0 mm

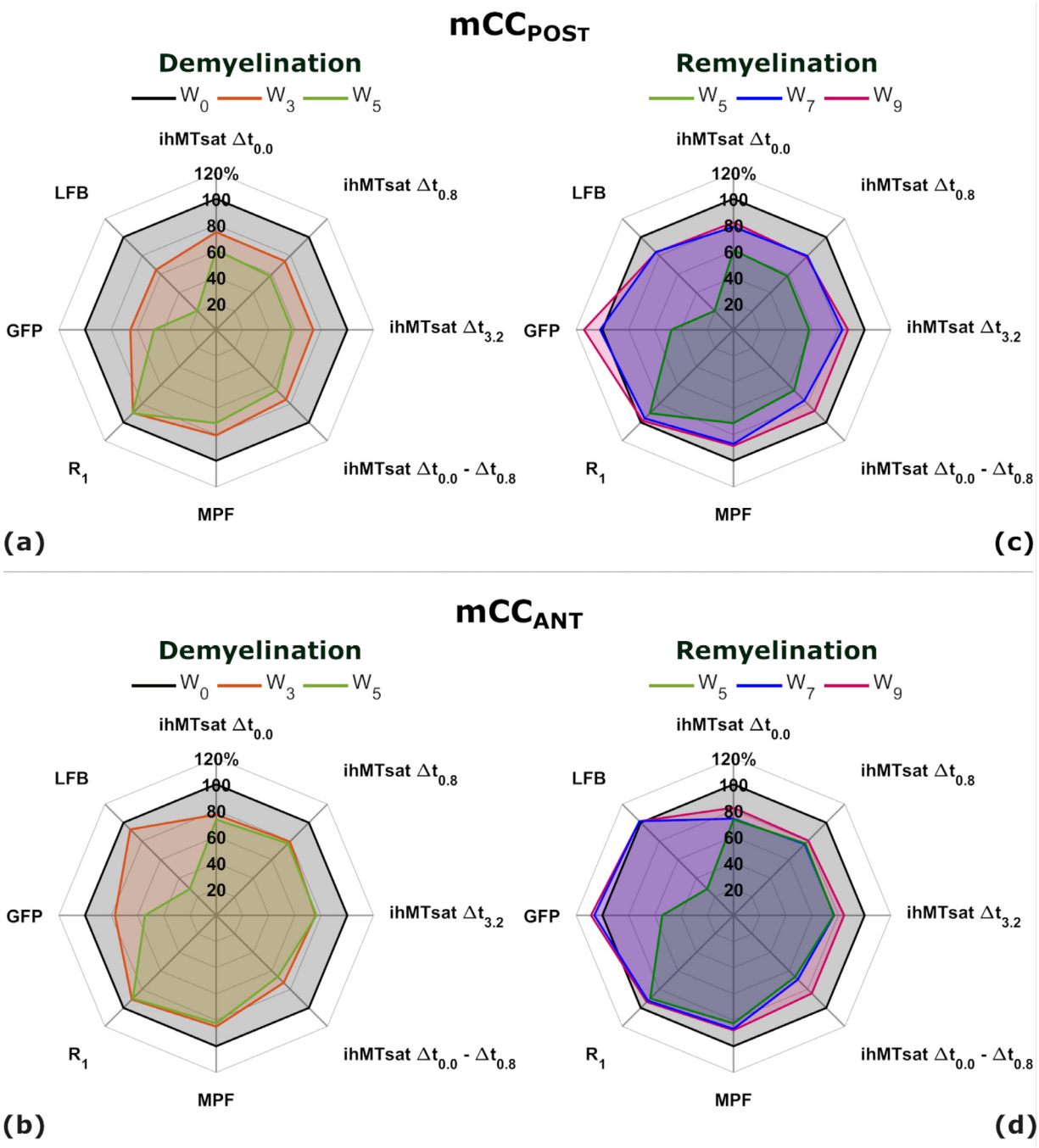

Fig. 7. Relative evolution of all the investigated metrics with respect to W_0 in mCC_{POST} (a,c) and mCC_{ANT} (b,d) during the demyelination (W_0-W_3-W_5; a,b) and remyelination (W_5-W_7-W_9; c,d) phases of the cuprizone model. The signal at W_0 was added on the remyelination radar plots to better appreciate the incomplete signal recovery of the investigated metrics.

from bregma) of the mCC, except for R_1 (Fig. 10e) which shows a rather flat profile along the whole mCC. Thus, the other MRI metrics present moderate spatial and temporal variations (ihMT T_{1D}-filters) or even a rather stable signal loss (MPF) across the rostral mCC, while in contrast, a progressive increase in signal loss is observed for all MRI metrics caudally, with a maximum reached between – 1.1 mm and – 1.5 mm from bregma, depending on the metric. In terms of amplitude, the signal loss in the caudal part reached values of up to 2 to 3 times higher than those measured in the rostral part for ihMT high-pass T_{1D}-filters and MPF (Fig. 10a-e, W_5, blue curves). The highest signal loss was obtained at the demyelination peak (W_5) for ihMT high-pass T_{1D}-filters with a clear trend for higher amplitude as the filter becomes more specific to myelination (δihMTsat $\Delta t_{0.0}$ = -37% vs. δihMTsat $\Delta t_{3.2}$ = -47%). In contrast, the maximum signal loss was only -30% for MPF and the ihMT band-pass T_{1D}-filter, and -8% for R_1. Also, in contrast to ihMT T_{1D}-filters, one should note the limited amplitude of signal loss observed with MPF rostrally at W_5 as highlighted by the similar levels of green (W_3) and blue (W_5) curves (Fig. 10e).

Greater amplitude changes during recovery – which can be assessed by the difference between the blue curves (W_5) and the orange curves (W_9) – were also observed caudally in the mCC for the ihMT high-pass T_{1D}-filters (Fig. 10a-c) and MPF (Fig. 10e). For the ihMT band-pass T_{1D}-filter and R_1 the changes during recovery in the rostral and caudal parts of the mCC were very close. None of the metrics except for the ihMT

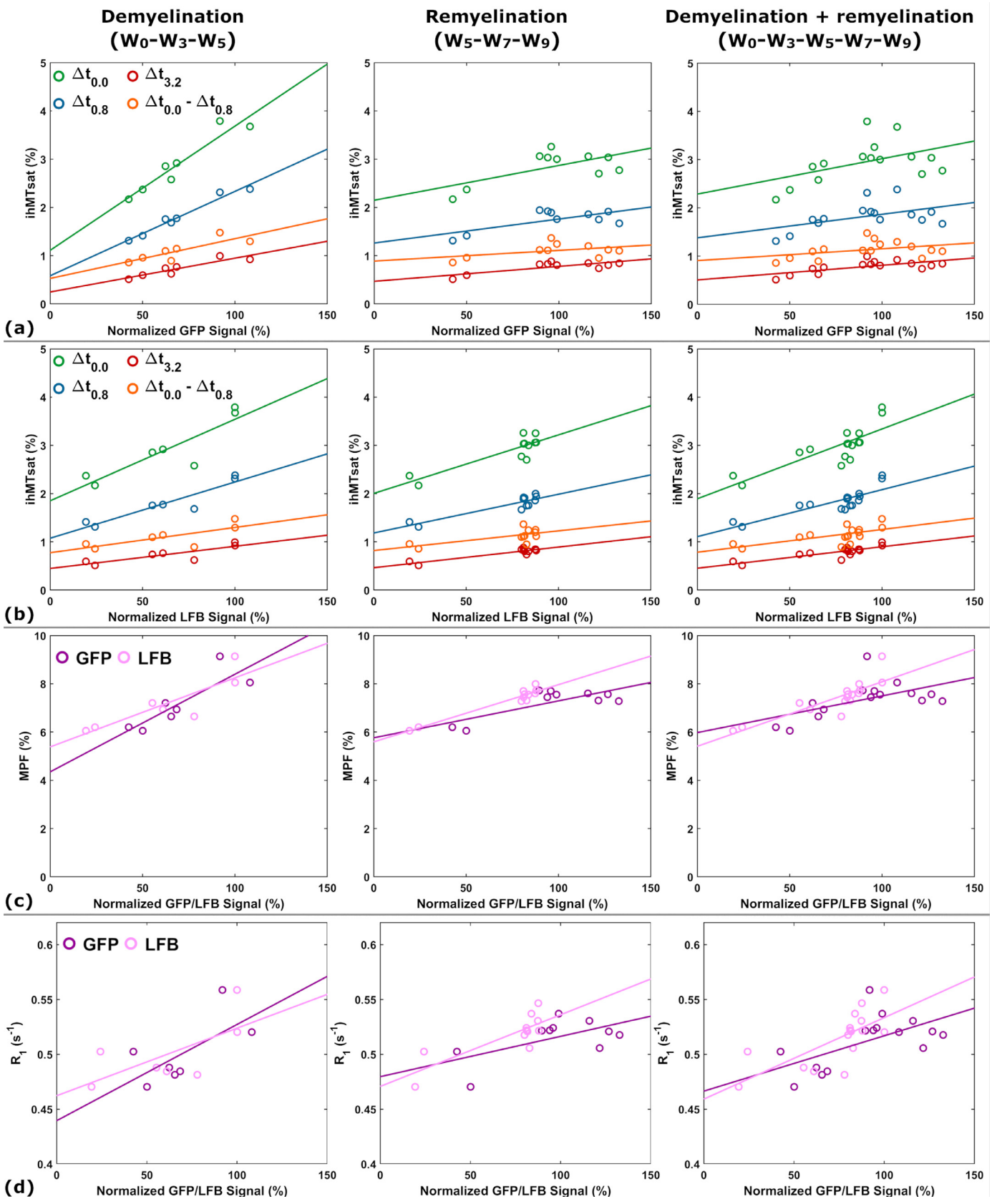

Fig. 8. Plots of linear regression analyses between the MRI and histology metrics in mCC_{POST}. Each point corresponds to the mean value in the mCC_{POST} ROI for one mouse. The data points at W_5 ($N_{W5} = 2$ mice) appear in both the demyelination and the remyelination plots. .

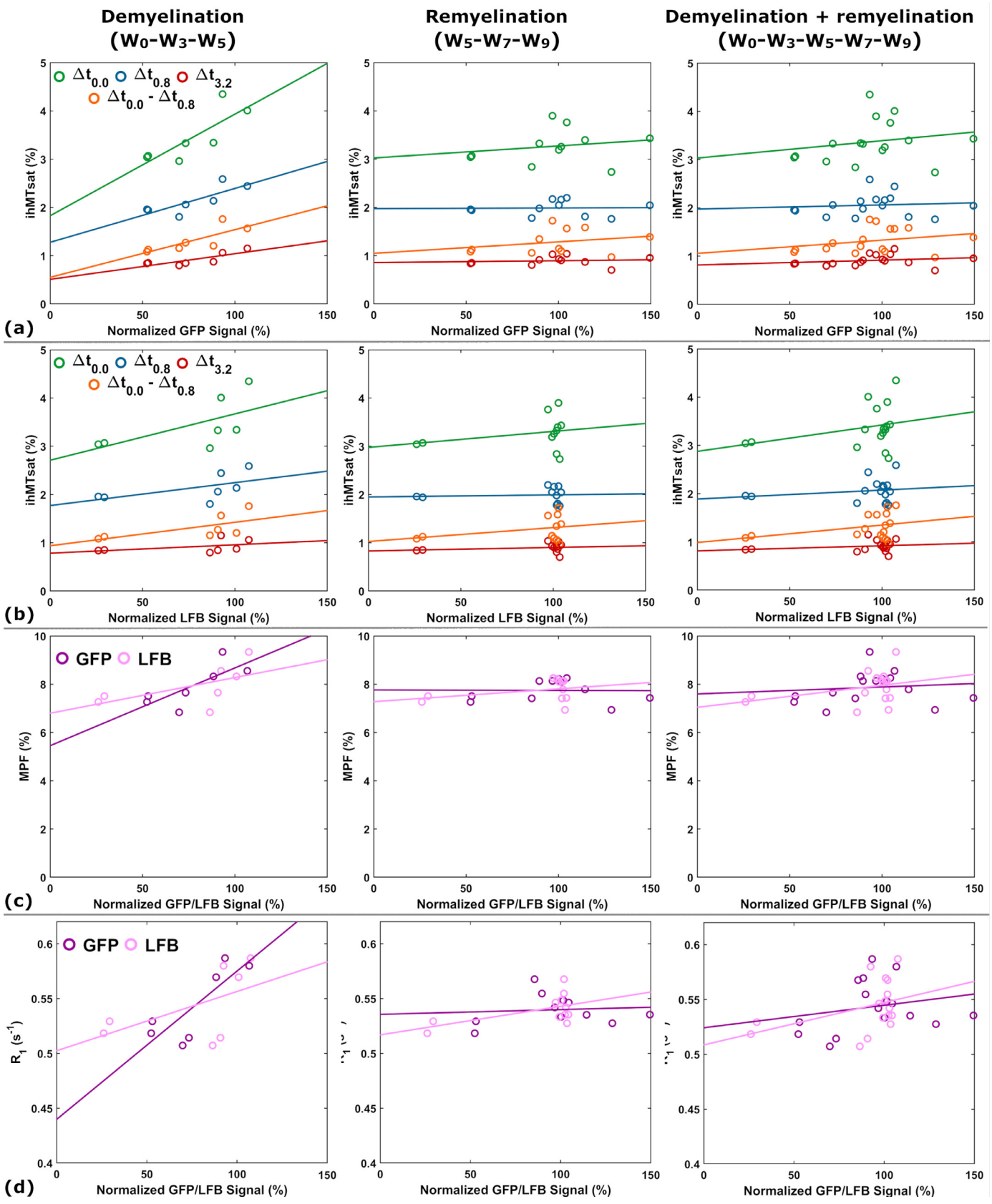

Fig. 9. Plots of linear regression analyses between the MRI and histology metrics in mCC_{ANT}. Each point corresponds to the mean value in the mCC_{ANT} ROI for one mouse. The data points at W_5 ($N_{W5} = 2$ mice) appear in both the demyelination and the remyelination plots.

Table 3
Correlation coefficients (r^2) for associations between all MR metrics and the GFP and LFB signals during the demyelination and remyelination phases in the anterior (mCC_{ANT}) and posterior (mCC_{POST}) medial callosal structure. The asterisk sign indicates a significant correlation coefficient (*p-value* < 0.05).

Phase	Structure	Reference biomarker	ihMTsat $\Delta t_{0.0}$	ihMTsat $\Delta t_{0.8}$	ihMTsat $\Delta t_{3.2}$	ihMTsat $\Delta t_{0.0}$-$\Delta t_{0.8}$	MPF	R_1
Demyelination (W_0-W_3-W_5)	mCC_{ANT}	GFP	**0.66***	**0.65***	**0.67***	**0.63***	**0.59***	**0.67***
		LFB	0.37	0.32	0.19	0.42	0.34	0.29
	mCC_{POST}	GFP	**0.91***	**0.96***	**0.84***	**0.71***	**0.72***	0.45
		LFB	**0.79***	**0.87***	**0.73***	**0.58***	**0.74***	0.45
Remyelination (W_5-W_7-W_9)	mCC_{ANT}	GFP	0.04	0.00	0.01	0.07	0.00	0.01
		LFB	0.08	0.01	0.05	0.11	0.12	0.32
	mCC_{POST}	GFP	**0.41***	**0.47***	**0.62***	0.20	**0.59***	0.36
		LFB	**0.77***	**0.83***	**0.86***	**0.48***	**0.93***	**0.67***
Entire dynamics (W_0-W_3-W_5-W_7-W_9)	mCC_{ANT}	GFP	0.04	0.01	0.05	0.08	0.01	0.05
		LFB	0.10	0.04	0.05	0.13	0.13	0.17
	mCC_{POST}	GFP	0.23	0.24	**0.45***	0.16	**0.32***	**0.36***
		LFB	**0.65***	**0.71***	**0.72***	**0.43***	**0.72***	**0.51***

Table 4
Comparisons between the correlation coefficients (r^2) reported in Table 3 for associations between the GFP/LFB signals and a single MRI metric for the demyelination, remyelination phases and the entire signal dynamics in mCC_{POST}. Comparisons were only made for the pairs of statistically significant correlation coefficients. The asterisk sign indicates the significant coefficient (p-value < 0.05).

Phase	ihMT high-pass and band-pass T_{1D}-filters				MPF	R_1
	ihMTsat $\Delta t_{0.0}$	ihMTsat $\Delta t_{0.8}$	ihMTsat $\Delta t_{3.2}$	ihMTsat $\Delta t_{0.0}$ - $\Delta t_{0.8}$		
Demyelination (W_0-W_3-W_5)	0.34 [-0.14, 0.51]	0.19 [-0.04, 0.37]	0.47 [-0.26, 0.58]	0.49 [-0.38, 0.72]	0.94 [-0.51, 0.47]	–
Remyelination (W_5-W_7-W_9)	**0.04* [-0.80, -0.02]**	**0.03* [-0.76, -0.04]**	0.12 [-0.58, 0.05]	–	**< 0.001* [-0.70, -0.07]**	**–**
Entire dynamics (W_0-W_3-W_5-W_7-W_9)	**–**	**–**	0.13 [-0.56, 0.06]	–	**0.03 [-0.71, -0.04]**	0.41 [-0.51, 0.19]

band-pass T_{1D}-filter in rostral regions seem to completely recover to the baseline signal levels ($\delta Metric_{W9} < 0$ at W_9). On the other hand, the positive values of δihMTsat at W_7 around the bregma, and at W_9 in the rostral mCC for the band-pass T_{1D}-filter indicate a level of signal recovery above that of the baseline.

3.3. Voxel-wise statistical analyses in the entire acquired volume

Results of the VBM analysis for the demyelination and remyelination phases are presented in Fig. 11. Significant signal variations are mostly localized in the CC and to some extent, in the CTX (Fig. 11a). More importantly, in addition to the rostro-caudal gradients during demyelination, medio-lateral gradients can be noticed as well for the ihMT high-pass T_{1D}-filters. Less statistically significant voxels were found for MPF, most likely due to its lower myelin specificity (Hertanu et al., 2022b), while no statistically significant voxels were found in the lateral CC for the band-pass T_{1D}-filter. Finally, no statistically significant voxels were found for R_1. Statistically significant voxels during the remyelination phase were found caudally in the mCC for the ihMT high-pass T_{1D}-filters and MPF. For the latter, few statistically significant voxels in the rostral part of the lateral CC were also found. Finally, no statistically significant remyelination voxels were found for the ihMT band-pass T_{1D}-filter or R_1.

4. Discussion

The present study investigated the association of several ihMTsat variants corresponding to a different T_{1D} weighting, MPF and R_1 with the toxin-induced variations in the myelin content of mice subjected to an acute cuprizone intoxication. The main findings can be summarized as: i) All metrics except R_1 show significant variations in the mCC consistent with the effects generated by the cuprizone diet – a signal decrease during the demyelinating intoxication phase followed by a signal recovery during remyelination in the weeks resuming a normal diet (Matsushima and Morell, 2001; Hiremath et al., 1998; Morell et al., 1998; Mason et al., 2001); ii) IhMT signals associated with long T_{1D}s (high-pass T_{1D}-filters) present the highest signal loss at the demyelination peak (W_5) and correlate strongly and significantly with the myelin content assessed by GFP and LFB staining during both the demyelination and remyelination phases. Concurrently, ihMT signals associated with shorter T_{1D}s in the 100 μs to 1 ms range (band-pass T_{1D}-filter) show weaker or non-significant correlations. iii) Despite MPF showing strong correlation coefficients with histology comparable with the ihMT high-pass T_{1D}-filters, a better capability for the characterization of the spatial-temporal extent of demyelination and remyelination (e.g., rostro-caudal profiles of demyelination in the mCC described in the literature (Steelman et al., 2012)) of the acute cuprizone model was obtained for the ihMT high-pass T_{1D}-filters.

4.1. Sensitivity of ihMT high-pass T_{1D}-filters to the cuprizone-induced demyelination

Multiple studies have demonstrated increased severity of the induced demyelination in the caudal part of the medial corpus callosum as compared to the rostral part by means of histology or MRI techniques (Steelman et al., 2012; Stidworthy et al., 2006; Khodanovich et al., 2017; Wu et al., 2008; Xie et al., 2010; Tagge et al., 2016; Yang et al., 2009; Binder et al., 2008). Results obtained in this study for ihMT support these findings. For example, a factor of 2 in signal drop can be observed at the demyelination peak (W_5) between mCC_{POST} and mCC_{ANT} for the $\Delta t_{3.2}$ high-pass T_{1D}-filter. Furthermore, the two histology metrics investigated in this study, namely GFP and LFB, corroborate with the strong signal decrease in mCC_{POST} during the demyelination phase. Additionally, the good agreement between GFP and LFB histology measurements and the ihMT high-pass T_{1D}-filters and MPF in the mCC_{POST} during demyelination is emphasized by their corresponding high correlation coefficients ($r^2 \geq 0.72$, *p-value* < 0.05).

However, results obtained in mCC_{ANT} for histology metrics are more surprising. Both GFP and LFB quantifications present a signal drop of equivalent magnitude in mCC_{ANT} as compared to mCC_{POST}.

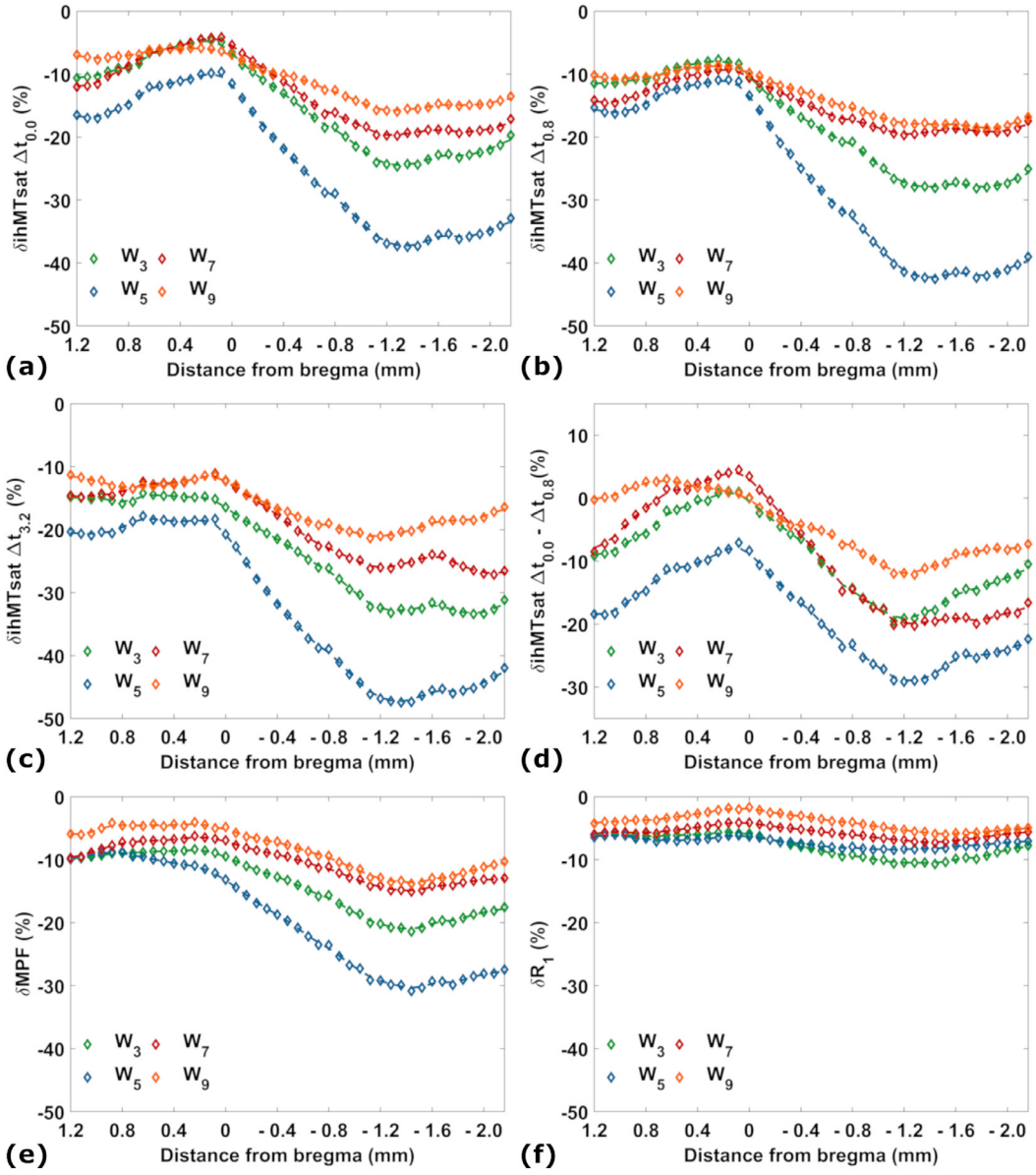

Fig. 10. Spatial-temporal profiles of signal loss for (a-c) ihMT high-pass T_{1D}-filters, (d) ihMT band-pass T_{1D}-filter, (e) MPF and (f) R_1 measured in the medial CC during the demyelination and remyelination phases of the cuprizone mouse model. The signal variation for each time point is expressed as a percentage relative to initial time point (W_0) and demonstrates the heterogeneity of the demyelination and the remyelination processes along the rostro-caudal axis. (For interpretation of the references to colour in this figure legend, the reader is referred to the web version of this article.)

These results are in contradiction with the complex patterns of demyelinating gradients reported in the literature (Steelman et al., 2012; Stidworthy et al., 2006; Khodanovich et al., 2017; Wu et al., 2008; Xie et al., 2010; Tagge et al., 2016; Yang et al., 2009; Binder et al., 2008) and our own MR findings which clearly demonstrate a significantly higher signal loss in mCC_{POST} as compared to mCC_{ANT}. At this stage, we do not have a precise explanation for these results, although an issue in the process of chemical fixation for the brain slices at bregma + 0.7 mm or the highly localized nature of histological analyses cannot be excluded as possible biases. As a result, the relatively lower or non-significant correlation coefficients obtained for mCC_{ANT} between histological and MRI metrics in this study should be considered and interpreted with great caution.

4.2. Correlation of ihMT high-pass T_{1D}-filters with GFP and LFB signals

Despite their current use as reference methods, protein and lipid biomarkers are also prone to confounding factors that limit their tissue specificity and sensitivity. Therefore, the agreement between MRI metrics and histology quantifications is highly dependent on the employed histological biomarker as well as the tissue preparation protocol (Lazari and Lipp, 2021). In addition, histological and MRI methods have different spatial resolutions, microscopic versus mesoscopic, respectively. This makes impossible a perfect match in the analyzed ROIs between the two modalities.

That being said, LFB staining has demonstrated high reliability for the detection of the demyelination and remyelination processes in the mCC in the cuprizone mouse model when compared to electron microscopy (EM) (Lindner et al., 2008), despite the false-positive signals arising from myelin lipid debris (Matsushima and Morell, 2001). To a lesser extent, various myelin proteins were shown to describe the demyelination process using immunohistochemical staining (Lindner et al., 2008).

In the present study, a fluorescent biomarker, the GFP co-expressed with the PLP, was employed. GFP was shown to be an excellent myelin proxy for healthy tissues in the adult mouse brain (Ferent et al., 2013),

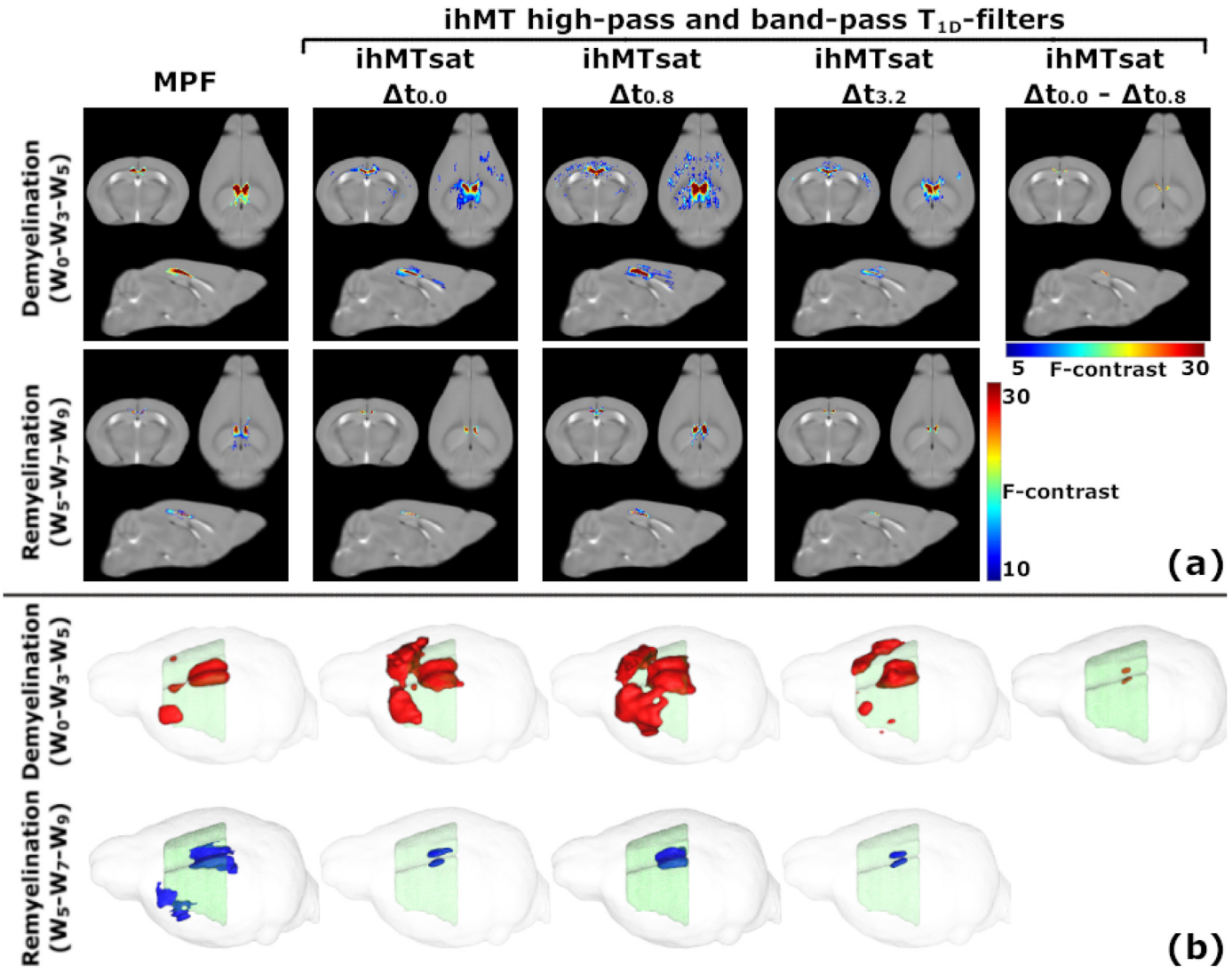

Fig. 11. VBM results. (a) Voxels with significant signal variations (*p-value* < 0.01) for MPF, ihMT high-pass and band-pass T_{1D}-filters are overlayed on top of representative T_2w images in the three directions of space. The F-contrast indicates the strength of significance for each voxel (higher F-values correspond to lower *p-values*). During demyelination significant voxels can be observed in other structures than the corpus callosum, but the significance level (*p-value*) is lower. During remyelination most of the significant voxels are located in the corpus callosum. (b) Significant clusters during the demyelination (red) and remyelination (blue) phases for the same MRI metrics are illustrated in three dimensions for a comprehensive description of the demyelination and remyelination extent. (For interpretation of the references to colour in this figure legend, the reader is referred to the web version of this article.)

providing superior robustness as compared to PLP antibodies. Although no EM measurements were performed in our study, the high correlation coefficient obtained during the demyelination phase in mCC_{POST} between LFB and GFP ($r^2 = 0.85$, *p-value* < 0.05, data not shown) suggests a good agreement between these two markers. Furthermore, the strong and non-significant different correlation coefficients for associations of the ihMT high-pass T_{1D}-filters with either GFP or LFB during the demyelination phase, clearly denote ihMT high-pass T_{1D}-filters as suitable *in vivo* biomarkers for the demyelination process.

On the other hand, the early synthesis of myelin proteins such as MBP and PLP after cuprizone diet withdrawal when there is only little remyelination according to EM analyses (Lindner et al., 2008), renders protein-based markers less trustworthy to characterize the remyelination process. Consistent with this logic, our study found that the correlation coefficient between GFP and LFB for the remyelination phase in mCC_{POST} was lower ($r^2 = 0.77$, *p-value* < 0.05, data not shown) compared to the demyelination phase. Importantly, correlation coefficients obtained for associations between the ihMT high-pass T_{1D}-filters ($\Delta t_{0.0}$ and $\Delta t_{0.8}$) and LFB were statistically higher than with GFP (Table 4). These results are highly encouraging and demonstrate that ihMT high-pass T_{1D}-filters are pertinent for the *in vivo* evaluation of remyelination mechanisms. As expected, when considering the entire signal dynamics (demyelination + remyelination), correlation coefficients are lower due the disagreement between MRI and histology metrics during the remyelination phase.

4.3. Sensitivity of ihMT high-pass T_{1D}-filters to remyelination

When comparing the signal amplitudes at W_0 and W_9, a different behavior is observed between the histology metrics, tending to a complete (GFP) or nearly complete (LFB) recovery, and the MR-based metrics showing a partial signal recovery only.

It has been previously shown that most of the protein content is restored to baseline after only few days following cuprizone withdrawal (Lindner et al., 2008), thus explaining the complete recovery of the GFP signal in this study. Also in line with our LFB results, previous studies have shown that two-thirds of the LFB signal is restored within two weeks following cuprizone withdrawal and the signal recovery is nearly

complete after six weeks (Lindner et al., 2008). However, the initial state of the myelin is not fully restored since a lower percentage of myelinated axons is found by EM (Stidworthy et al., 2006; Merkler et al., 2005) even after ten weeks of normal diet (Mason et al., 2001; Lindner et al., 2008). In addition, a less structured and compact appearance of the newly regenerated myelin (Lindner et al., 2008; Gonsalvez et al., 2019) with a clear impact on its functionality (Skripuletz et al., 2011; Lindner et al., 2008) was reported. All these aspects may modulate the amplitude and frequency of the membrane collective motions, leading to a potential reduction of the average T_{1D} as compared to that of normal myelin. The incomplete signal recovery observed for the ihMT high-pass T_{1D}-filters (Hertanu et al., 2022a) would

Future investigations should include EM analyses to evaluate the myelin ultrastructure in order to confirm this hypothesis and to evaluate the potential of ihMT to distinguish between healthy and remyelinated tissues.

4.4. Rostro-caudal gradient of demyelination and remyelination in the medial cc

Rostro-caudal gradients of demyelination and remyelination along the mCC have been made apparent by histology studies (Steelman et al., 2012; Stidworthy et al., 2006). In a study investigating the extent of demyelination in C57BL/6 mice fed with 0.2% cuprizone for five weeks, and that of remyelination after two subsequent weeks of normal diet, Steelman et al. (Steelman et al., 2012) showed a minimum demyelination near the bregma (~ + 0.5 mm), and roughly thrice more important in the caudal part of the mCC (< - 1.0 mm from bregma) compared to that of the rostral part (> + 1.0 mm from bregma). This gradient diminished after two weeks of recovery, tending toward control results for which no remarkable rostro-caudal profile is noticeable, hence indicating a more important remyelination of the caudal mCC. Previous attempts to highlight such a gradient with myelin sensitive MRI techniques, including diffusion-based techniques (Wu et al., 2008; Xie et al., 2010; Song et al., 2005), MTR (Tagge et al., 2016), and MPF (Khodanovich et al., 2017) have reported mixed results. For example, one study demonstrated an increase in the radial diffusivity by approximately 18% in the caudal part of the mCC relative to the rostral part after four weeks of cuprizone treatment (Wu et al., 2008), while in another study no variation was found for the same metric and the same time of cuprizone administration (Xie et al., 2010). The concurrence of axonal pathologies that possibly reduced the sensitivity of diffusion metrics in assessing the extent of demyelination was advanced as a plausible explanation for this discrepancy.

Regarding MT-based studies, a very small variation of MTR (~2% absolute units) has been found between the rostral and caudal aspects of the mCC after six weeks of cuprizone diet (Tagge et al., 2016), whereas no significant difference in MPF along the rostral-caudal direction was noticed after eight weeks of cuprizone administration (Khodanovich et al., 2017). If the elevated microgliosis and astrogliosis present in the caudal regions (Tagge et al., 2016) can contribute to MTR values and likely counterbalance the MTR decrease due to demyelination, the absence of MPF variations is more surprising since this quantitative metric, independent of the MR acquisition parameters, has shown higher sensitivity to myelin density compared to MTR (Underhill et al., 2011). In contrast, our MPF results (Fig. 10e) indicate a clear distinction along the rostro-caudal direction. As proposed by the authors (Khodanovich et al., 2017), the long time period of the cuprizone diet may have induced a more extensive homogeneous demyelination in that study, therefore not contradicting our results.

In our study, R_1 shows very little variation along the rostro-caudal axis (Fig. 10f). However, the dependency of the estimated R_1 on the measurement technique is well documented in the literature as well as the tendency of the VFA approach to overestimate the longitudinal relaxation time (T_1) when compared to the reference Inversion Recovery (IR) method (Stikov et al., 2015). This raises the question as to whether another R_1 quantification approach would have led to different results. Despite the various biases influencing the VFA method, the derived R_1 maps in the current analyses were corrected for B_1^+ inhomogeneity effects based on the dedicated AFI B_1^+ map and an optimized gradient RF spoiling scheme has been applied. Although an IR-based technique would have likely led to different absolute R_1 values, we anticipate marginal changes in the low R_1 signal variations during the demyelination and remyelination phases because the systematic errors encountered in T_1 measurements are not dominating the overall T_1 contrast which is driven by common contrast mechanisms.

On the other hand, the R_1 contrast is known to be affected by a large range of factors, from the overall macromolecular content (Manning et al., 2021), to tissue hydration (Filo et al., 2019) and the presence of paramagnetic ions (Lauffer, 1987). For example, copper accumulation in the corpus callosum of mice as a consequence of the cuprizone diet might induce a counteractive effect to that produced by the demyelination mechanisms. However, this is merely a speculation, since both copper deficiency and copper buildup in the brain seem to be equally viable hypotheses to explain the physico-chemical behavior of cuprizone (Praet et al., 2014). Some studies argue that the levels of copper in the brain remain stable during the cuprizone diet (Moldovan et al., 2015), but no quantifications were performed in the corpus callosum. On the other hand, the accumulation of glial cells, the most iron-rich cells in the brain (Reinert et al., 2019), at the site of demyelination is another potential explanation for the small variations observed in R_1.

The rostro-caudal profiles obtained in this study for the ihMT high-pass T_{1D}-filters at W_5 and W_7 (Fig. 10a-c) correspond strikingly to the results advanced by Steelman et al. (Steelman et al., 2012) for histological myelin staining quantifications. Indeed, the ihMT high-pass T_{1D}-filters capture both a minimal demyelination close to bregma level, the 2- to 3-fold difference in demyelination between the rostral and caudal mCC (W_5) as well as the greater remyelination of the caudal mCC (W_7). In contrast to ihMT, MPF showed weaker sensitivity to demyelination of the rostral mCC (> + 0.8 mm), as indicated by the relatively similar MPF values between W_3 and W_5. However, the signal decreases even for the most myelin-specific ihMT protocol (ihMTsat $\Delta t_{3.2}$) remain less substantial than the complete signal loss observed by histology (Steelman et al., 2012). Beyond the potential smoothing effect due to much large voxel size of MRI data, a plausible explanation for the limited capability of ihMT high-pass T_{1D}-filters to reflect a complete demyelination could be the presence of lipid debris in the demyelinated area (Steelman et al., 2012; Matsushima and Morell, 2001). Indeed, the strong correlation of ihMT high-pass T_{1D}-filters with the LFB signal prone to overestimation induced by myelin debris, suggests a sensitivity of ihMT to myelin debris as well. In addition, demyelination and microglial infiltration have similar patterns in the mCC (Hiremath et al., 1998; Matsushima and Morell, 2001; Wu et al., 2008; Xie et al., 2010; Tagge et al., 2016), thus influencing the size of the macromolecular content in opposite directions and obscuring myelin-related events for any metric sensitive to the macromolecular content. As microglia tend to have shorter T_{1D} molecules, this effect would affect more the ihMT signals that weakly filter the short T_{1D} component. All combined, the effects of microglia would be in line with the lower variations observed with MPF, ihMTsat $\Delta t_{0.0}$ and ihMTsat $\Delta t_{0.8}$ compared to that of ihMTsat $\Delta t_{3.2}$.

4.5. The ihMT band-pass T_{1D}-filter in the cuprizone model

Multiple differences can be noticed between the behavior of the ihMT high-pass and band-pass T_{1D}-filters in ROI-wise and voxel-wise analyses. However, interpretations for the band-pass T_{1D}-filter are less straightforward. Previous work on healthy mice has demonstrated that the short T_{1D} components correlate less with LFB and GFP fluorescence (Hertanu et al., 2022b). Hence, if the signal variations for the ihMT band-pass T_{1D}-filter in the cuprizone model are to a lesser extent sensitive to the demyelination and remyelination mechanisms, they may also reflect other processes reported in the cuprizone model including

myelin debris (Steelman et al., 2012; Matsushima and Morell, 2001; Lindner et al., 2008) and infiltration of glial cells and macrophages (Steelman et al., 2012; Tagge et al., 2016), all expected to be associated with shorter T_{1D} values. Future studies with a more extensive histological analysis will be needed to further clarify the exact origin of the short T_{1D} components and their respective sensitivity to the different mechanisms taking place in the cuprizone model.

4.6. Medio-lateral gradients of demyelination and remyelination in the cc

Medio-lateral gradients during demyelination were previously reported for MTR and histology quantifications (Tagge et al., 2016), as well as MPF (Khodanovich et al., 2017).

In this work, VBM analyses of the ihMT high-pass T_{1D}-filters exhibited statistically significant voxels during demyelination in the lateral part of the rostral CC along with those in the medial part of the caudal CC, thus highlighting the medio-lateral and rostro-caudal gradients of demyelination. However, results obtained for the ihMTsat $\Delta t_{3.2}$ were somewhat surprising. By increasing the signal contribution of long T_{1D}s and thus the specificity to myelination (Hertanu et al., 2022b), a higher number of significant voxels is detected when comparing the $\Delta t_{0.0}$ and the $\Delta t_{0.8}$ configurations. This is however not the case when Δt is further lengthened to 3.2 ms. Voxel-wise analyses are highly dependent on the SNR and the ihMT high-pass T_{1D}-filter with the longest Δt value suffers from low SNR, thus possibly biasing the comparison. Similarly, SNR issues may have impaired the band-pass T_{1D}-filter VBM analysis which shows the lowest number of statistically significant voxels.

4.7. Spatial extent of demyelination and remyelination in the acute cuprizone mouse model

Several MRI studies including various time periods of cuprizone administration have reported demyelination in other WM structures such as the anterior commissure, the optic tracts or the internal (IC) and external (EC) capsules (Vega-Riquer et al., 2019; Khodanovich et al., 2017; Song et al., 2005), but to a lesser extent than in the CC. Although our MRI/histology ROI analyses were restrained to the medial corpus callosum and the cerebral cortex, the VBM analyses highlight a few significant voxels during the demyelination phase in IC and EC for ihMT high-pass T_{1D}-filters, but with a weaker significance strength (Fig. 11a). These results are promising and demonstrate the potential of myelin-specific ihMT protocols to further study the extent of abnormal voxels over the whole brain.

In the current study we also investigated the signal dynamics of ihMT T_{1D}-filters in the cerebral cortex as cortical GM demyelination is a characteristic feature of the cuprizone model (Skripuletz et al., 2011). Results and discussion related to the cerebral cortex are provided in Supplementary Information.

4.8. Limitations

A major limitation in this study was the lack of histology biomarkers specific to other mechanisms taking place during the demyelination and remyelination phases, such as astrogliosis and microgliosis, presumably associated with short T_{1D} components and which should then contribute differently to the signal of ihMT high-pass and band-pass T_{1D}-filters. Such histology biomarkers along with electron microscopy analyses would help future studies in establishing the exact relationship between the short T_{1D} components and white matter microstructural components other than myelin, and in evaluating more accurately the capacity of ihMT to distinguish between a healthy and a repaired myelin sheath.

Furthermore, natural myelination processes related to brain development have not been considered although they might interfere with the evaluation of the various metrics. For example, MTR was shown to continue to increase in both the medial and the lateral corpus callosum of adult mice as a result of ongoing development and maturation (Tagge et al., 2016). Thus, an aged-matched cohort of mice during our nine-week study (as opposed to a baseline reference) might have been useful for a more rigorous evaluation of the remyelination phase as viewed by the MRI metrics.

Despite the consideration of the two groups of mice and the large amount of data generated in this study, the number of mice per time point was relatively small and thus probably limited the detectability of the voxel-wise analyses, especially for the lower SNR ihMT protocols, such as the $\Delta t_{3.2}$ high-pass T_{1D}-filter or the band-pass T_{1D}-filter. Therefore, it is not easy to interpret whether the lower number of statistically significant voxels for these 2 specific filters is due to underlying mechanisms or rather a technical limitation of the analysis itself.

5. Conclusion

To conclude, this study investigated the association of ihMT with the myelin alterations in the acute cuprizone mouse model. Multiple ihMT protocols sensitive to specific T_{1D} ranges were investigated. We showed that ihMT high-pass T_{1D}-filters, selective for long T_{1D} components, are specific and sensitive *in vivo* markers of demyelination and remyelination mechanisms. These ihMT T_{1D}-filters successfully captured the spatially heterogeneous pattern of the demyelination and remyelination phases and demonstrated a higher capability to characterize the spatial extent of myelin alterations compared to R_1 and MPF, two metrics sensitive but less specific to myelination. This study also underlined interesting differences in signal variations between the ihMT high-pass T_{1D}-filters and the band-pass T_{1D}-filter (selective for short T_{1D} components) and MPF, suggesting a sensitivity of the short T_{1D} components and the overall macromolecular fraction to alterations other than those of myelin. Some possible explanations concerning their nature were hypothesized, but future studies will need to further address these differences by examining more closely the origin of the short T_{1D} components and the variation of each T_{1D} component in pathology. The clinical value of ihMT in demyelinating diseases such as MS has only begun to be explored (Van Obberghen et al., 2018; Zhang et al., 2020). In the context where MS lesions are characterized by heterogeneous features (Lucchinetti et al., 2000), the present study emphasizes the potential of ihMT to reinforce multicontrast MRI studies (Merkler et al., 2005) for better diagnostic strategies.

6. Data availability statement

Data (Bruker format file) will be shared by request from any qualified investigator.

Data availability

Data will be made available on request.

Credit authorship contribution statement

Andreea Hertanu: Conceptualization, Methodology, Investigation, Formal analysis, Software, Writing – original draft. **Lucas Soustelle:** Methodology, Software, Writing – review & editing. **Julie Buron:** Formal analysis, Resources, Investigation. **Julie Le Priellec:** Formal analysis, Resources, Investigation. **Myriam Cayre:** Formal analysis, Investigation, Resources, Writing – review & editing. **Arnaud Le Troter:** Methodology, Software. **Valentin H. Prevost:** Writing – review & editing. **Jean-Philippe Ranjeva:** Writing – review & editing. **Gopal Varma:** Conceptualization, Writing – review & editing. **David C. Alsop:** Conceptualization, Writing – review & editing. **Pascale Durbec:** Resources, Writing – review & editing. **Olivier M. Girard:** Conceptualization, Methodology, Software, Writing – review & editing. **Guillaume**

Duhamel: Conceptualization, Funding acquisition, Project administration, Supervision, Writing – original draft.

Acknowledgements

This work was funded by ANR-17-CE18- 0030, the VERISMO project, and partly funded by France Life Imaging (Grant No. ANR-11-INBS-0006), ARSEP 2020, and CARNOT STAR 2020. We thank Nathalie Cuge for animal handling, Martine Armand and Christophe Vilmen for fruitful discussions, advice and help with the logistics of the cuprizone experiments.

Appendix

Appendix A. MRI maps for all the investigated time points during the demyelination and remyelination phases.

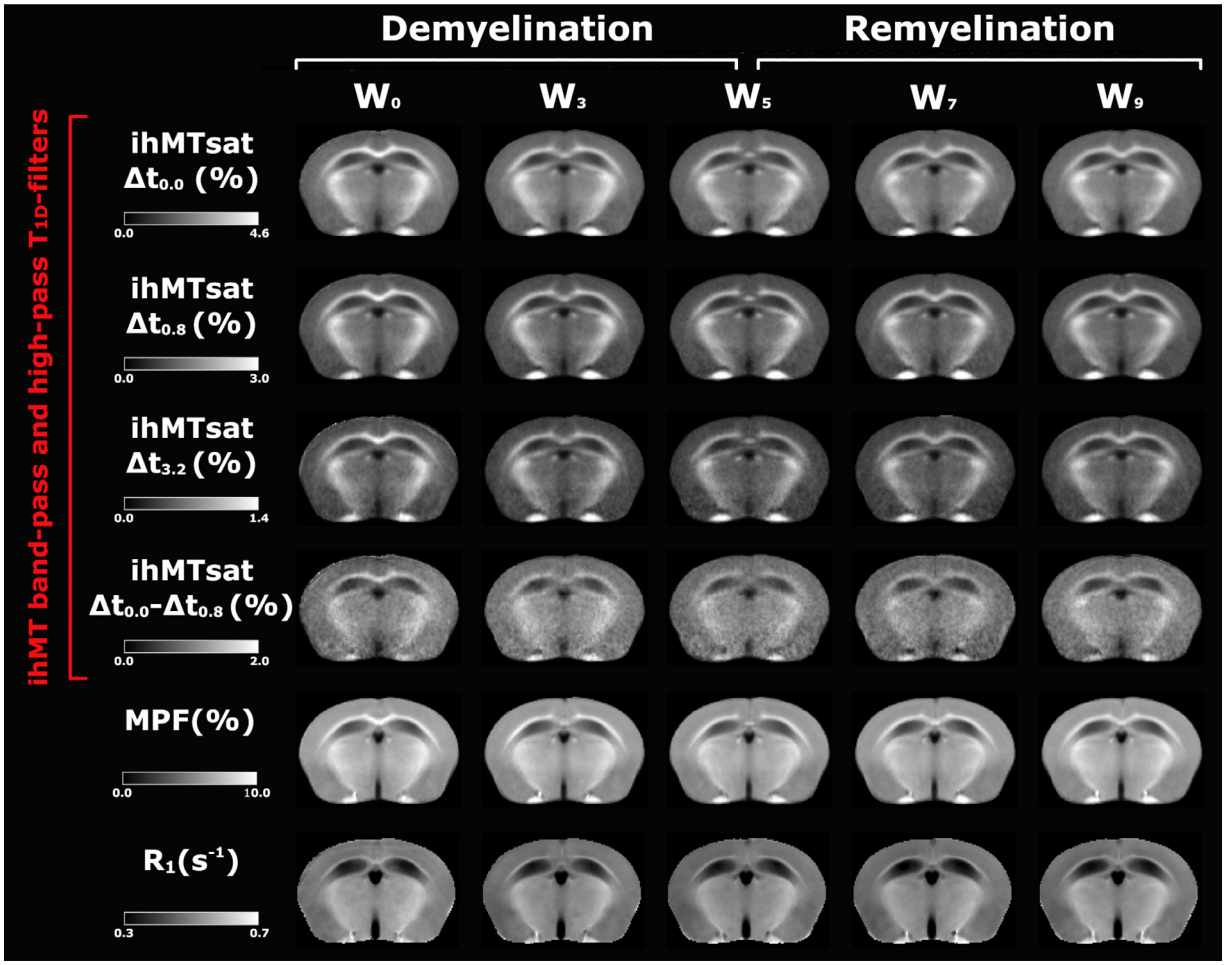

Fig. A1. Representative template-based posterior images (at – 1.0 mm from the bregma level) for ihMT high-pass (ihMTsat $\Delta t_{0.0}$, ihMTsat $\Delta t_{0.8}$ and ihMTsat $\Delta t_{3.2}$) and band-pass (ihMTsat $\Delta t_{0.0}$ - ihMTsat $\Delta t_{0.8}$) T_{1D}-filters, MPF and R_1 at the demyelination (W_0-W_3-W_5) and remyelination (W_5-W_7-W_9) time points.

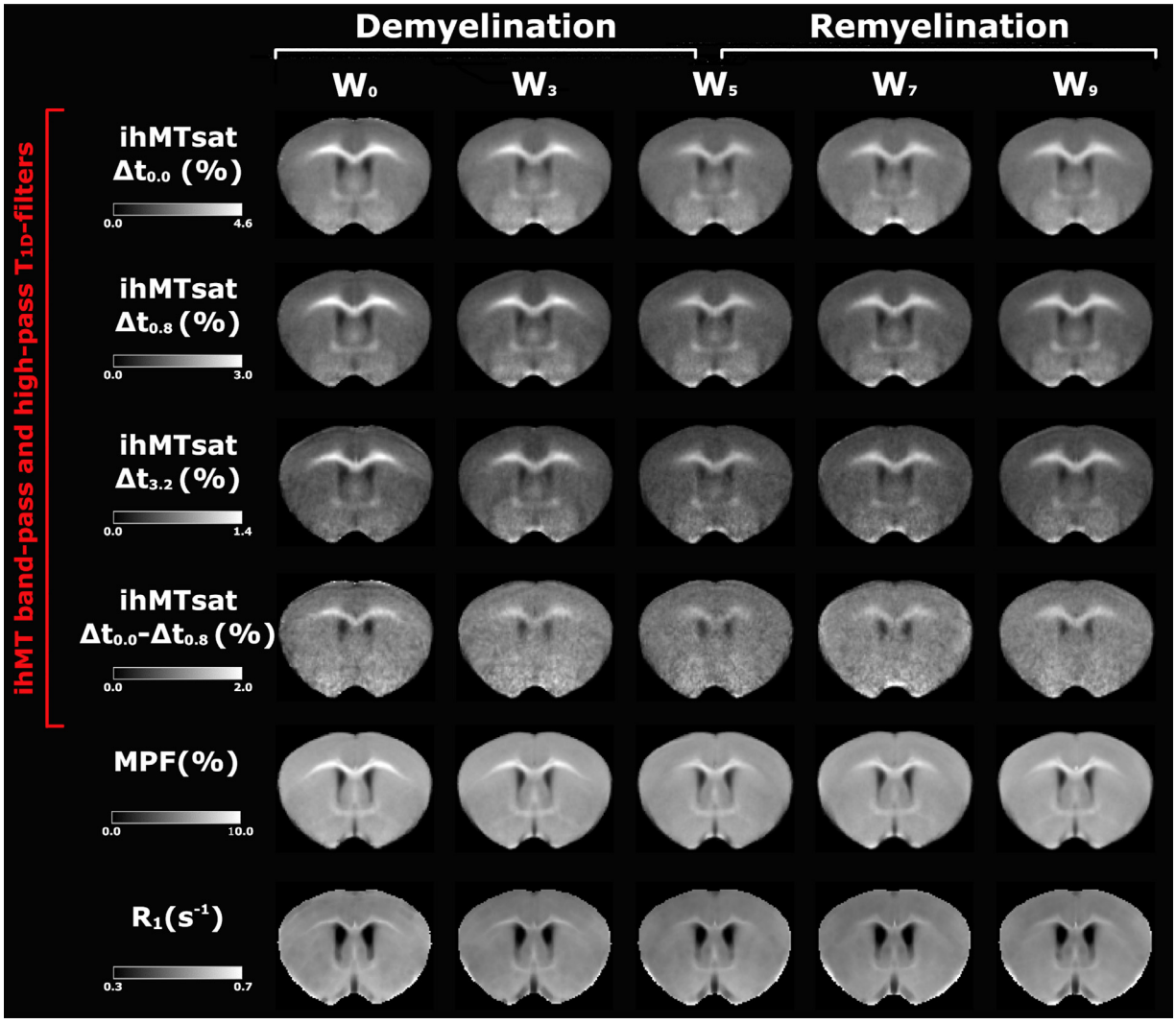

Fig. A2. Representative template-based anterior images (at + 0.7 mm from the bregma level) for ihMT high-pass (ihMTsat $\Delta t_{0.0}$, ihMTsat $\Delta t_{0.8}$ and ihMTsat $\Delta t_{3.2}$) and band-pass (hMTsat $\Delta t_{0.0}$ - ihMTsat $\Delta t_{0.8}$) T_{1D}-filters, MPF and R_1 at the demyelination (W_0-W_3-W_5) and remyelination (W_5-W_7-W_9) time points.

Supplementary materials

Supplementary material associated with this article can be found, in the online version, at doi:10.1016/j.neuroimage.2022.119785.

References

Avants, BB, Tustison, N, Song, G., 2009. Advanced Normalization Tools (ANTS). Insight J 2, 1–35.

Binder, MD, Cate, HS, Prieto, AL, Kemper, D, Butzkueven, H, Gresle, MM, et al., 2008 May 14. Gas6 Deficiency Increases Oligodendrocyte Loss and Microglial Activation in Response to Cuprizone-Induced Demyelination. J Neurosci 28 (20), 5195–5206.

Carvalho, VND, Hertanu, A, Grélard, A, Mchinda, S, Soustelle, L, Loquet, A, et al., 2020 Feb. MRI assessment of multiple dipolar relaxation time (T 1 D) components in biological tissues interpreted with a generalized inhomogeneous magnetization transfer (ihMT) model. J Magn Reson 311, 106668.

Chang, LC, Koay, CG, Basser, PJ, Pierpaoli, C., 2008 Aug. Linear least-squares method for unbiased estimation of T_1 from SPGR signals. Magn Reson Med 60 (2), 496–501.

Diedenhofen, B, Musch, J., 2015 Apr. cocor: A Comprehensive Solution For the Statistical Comparison of Correlations. PLOS ONE. 2;10(4):e0121945.

Dorr, AE, Lerch, JP, Spring, S, Kabani, N, Henkelman, RM., 2008 Aug. High resolution three-dimensional brain atlas using an average magnetic resonance image of 40 adult C57Bl/6 J mice. Neuroimage 42 (1), 60–69.

Dufourc, EJ, Mayer, C, Stohrer, J, Althoff, G, Kothe, G.Dynamics of phosphate head groups in biomembranes, 1992. Comprehensive analysis using phosphorus-31 nuclear magnetic resonance lineshape and relaxation time measurements. Biophys J 61 (1), 42–57 Jan.

Duhamel, G, Prevost, VH, Cayre, M, Hertanu, A, Mchinda, S, Carvalho, VN, et al., 2019 Oct. Validating the sensitivity of inhomogeneous magnetization transfer (ihMT) MRI to myelin with fluorescence microscopy. Neuroimage 199, 289–303.

Ferent, J, Ruat, M, Traiffort, E., 2013 Apr. Investigation of the proteolipid protein promoter activity during demyelination and repair. Differentiation 85 (4–5), 182–189.

Filo, S, Shtangel, O, Salamon, N, Kol, A, Weisinger, B, Shifman, S, et al., 2019 Jul 30. Disentangling molecular alterations from water-content changes in the aging human brain using quantitative MRI. Nat Commun 10 (1), 3403.

Gonsalvez, DG, Yoo, S, Fletcher, JL, Wood, RJ, Craig, GA, Murray, SS, et al., 2019 Nov 19. Imaging and Quantification of Myelin Integrity After Injury With Spectral Confocal Reflectance Microscopy. Front Mol Neurosci [Internet] 12. [cited 2021 May 18]Available from https://www.ncbi.nlm.nih.gov/pmc/articles/PMC6877500/.

Gudi, V, Gingele, S, Skripuletz, T, Stangel, M., 2014 Mar 13. Glial response during cuprizone-induced de- and remyelination in the CNS: lessons learned. Front Cell Neurosci [Internet] 8. [cited 2019 Aug 16]Available from https://www.ncbi.nlm.nih.gov/pmc/articles/PMC3952085/.

Höflich, KM, Beyer, C, Clarner, T, Schmitz, C, Nyamoya, S, Kipp, M, et al., 2016 Nov. Acute axonal damage in three different murine models of multiple sclerosis: a comparative approach. Brain Res 125–133 1650.

Hakkarainen, H, Sierra, A, Mangia, S, Garwood, M, Michaeli, S, Gröhn, O, et al., 2016. MRI relaxation in the presence of fictitious fields correlates with myelin content in normal rat brain. Magn Reson Med 75 (1), 161–168.

Hertanu, A, Soustelle, L, Le Troter, A, Buron, J, Le Priellec, J, Carvalho, VND, et al., 2022a. T1D-weighted ihMT imaging – Part I. Isolation of long- and short-T1D components by T1D-filtering. Magn Reson Med 87 (5), 2313–2328.

Hertanu, A, Soustelle, L, Buron, J, Le Priellec, J, Cayre, M, Le Troter, A, et al., 2022b. T1D-weighted ihMT imaging – Part II. Investigating the long- and short-T1D components correlation with myelin content. Comparison with R1 and the macromolecular proton fraction. Magn Reson Med 87 (5), 2329–2346.

Hiremath, MM, Saito, Y, Knapp, GW, Ting, JPY, Suzuki, K, Matsushima, GK., 1998 Dec 1. Microglial/macrophage accumulation during cuprizone-induced demyelination in C57BL/6 mice. J Neuroimmunol 92 (1), 38–49.

Janve, VA, Zu, Z, Yao, SY, Li, K, Zhang, FL, Wilson, KJ, et al., 2013 Jul. The radial diffusivity and magnetization transfer pool size ratio are sensitive markers for demyelination in a rat model of type III multiple sclerosis (MS) lesions. Neuroimage 74, 298–305.

Khodanovich, MY, Sorokina, IV, Glazacheva, VY, Akulov, AE, Nemirovich-Danchenko, NM, Romashchenko, AV, et al., 2017 Dec. Histological validation of fast macromolecular proton fraction mapping as a quantitative myelin imaging method in the cuprizone demyelination model. Sci Rep [Internet] 7 (1). [cited 2019 Mar 5]Available from http://www.nature.com/articles/srep46686.

Khodanovich, Pishchelko, Glazacheva, Pan, Akulov, Svetlik, et al., 2019 Oct 5. Quantitative Imaging of White and Gray Matter Remyelination in the Cuprizone Demyelination Model Using the Macromolecular Proton Fraction. Cells 8 (10), 1204.

Lauffer, RB., 1987. Paramagnetic Metal Complexes As Water Proton Relaxation Agents For NMR imaging: Theory and Design [Internet]. American Chemical Society [cited 2021 Jun 27]Available from.

Lazari, A, Lipp, I., 2021 Apr. Can MRI measure myelin? Systematic review, qualitative assessment, and meta-analysis of studies validating microstructural imaging with myelin histology. Neuroimage 230, 117744.

Lee, CH, Walczak, P, Zhang, J., 2022. Inhomogeneous magnetization transfer MRI of white matter structures in the hypomyelinated shiverer mouse brain. Magn Reson Med [Internet]. [citedApr 4]n/a(n/a)Available from https://onlinelibrary.wiley.com/doi/abs/10.1002/mrm.29207.

Lindner, M, Heine, S, Haastert, K, Garde, N, Fokuhl, J, Linsmeier, F, et al., 2008. Sequential myelin protein expression during remyelination reveals fast and efficient repair after central nervous system demyelination. Neuropathol Appl Neurobiol 34 (1), 105–114.

Lucchinetti, C, Brück, W, Parisi, J, Scheithauer, B, Rodriguez, M, Lassmann, H., 2000 Jun. Heterogeneity of multiple sclerosis lesions: implications for the pathogenesis of demyelination. Ann Neurol 47 (6), 707–717.

Manning, AP, Chang, KL, MacKay, AL, Michal, CA., 2017. The physical mechanism of "inhomogeneous" magnetization transfer MRI. J Magn Reson 274, 125–136 Jan.

Manning, AP, MacKay, AL, Michal, CA., 2021 Feb. Understanding aqueous and non-aqueous proton T1 relaxation in brain. J Magn Reson 323, 106909.

Mason, JL, Langaman, C, Morell, P, Suzuki, K, Matsushima, GK., 2001 Feb. Episodic demyelination and subsequent remyelination within the murine central nervous system: changes in axonal calibre. Neuropathol Appl Neurobiol 27 (1), 50–58.

Matsushima, GK, Morell, P., 2001. The Neurotoxicant, Cuprizone, as a Model to Study Demyelination and Remyelination in the Central Nervous System. Brain Pathol 11 (1), 107–116.

Mchinda, S, Varma, G, Prevost, VH, Le Troter, A, Rapacchi, S, Guye, M, et al., 2018 May. Whole brain inhomogeneous magnetization transfer (ihMT) imaging: sensitivity enhancement within a steady-state gradient echo sequence. Magn Reson Med 79 (5), 2607–2619.

Merkler, D, Boretius, S, Stadelmann, C, Ernsting, T, Michaelis, T, Frahm, J, et al., 2005. Multicontrast MRI of remyelination in the central nervous system. NMR Biomed 18 (6), 395–403.

Moldovan, N, Al-Ebraheem, A, Lobo, L, Park, R, Farquharson, MJ, Bock, NA., 2015 May 1. Altered transition metal homeostasis in the cuprizone model of demyelination. Neurotoxicology 48, 1–8.

Morell, P, Barrett, CV, Mason, JL, Toews, AD, Hostettler, JD, Knapp, GW, et al., 1998 Nov 1. Gene Expression in Brain during Cuprizone-Induced Demyelination and Remyelination. Mol Cell Neurosci 12 (4), 220–227.

Munsch, F, Varma, G, Taso, M, Girard, O, Guidon, A, Duhamel, G, et al., 2021 Jan. Characterization of the cortical myeloarchitecture with inhomogeneous magnetization transfer imaging (ihMT). Neuroimage 225, 117442.

Nyamoya, S, Schweiger, F, Kipp, M, Hochstrasser, T., 2017 Dec 1. Cuprizone as a model of myelin and axonal damage. Drug Discov Today Dis Models 63–68 25–26.

Paxinos, G, Franklin, KBJ., 2019. Paxinos and Franklin's The Mouse Brain in Stereotaxic Coordinates, 5th edition Elsevier Academic Press, San Diego.

Praet, J, Guglielmetti, C, Berneman, Z, Van der Linden, A, Ponsaerts, P., 2014 Nov. Cellular and molecular neuropathology of the cuprizone mouse model: clinical relevance for multiple sclerosis. Neurosci Biobehav Rev 47, 485–505.

Prevost, VH, Girard, OM, Mchinda, S, Varma, G, Alsop, DC, Duhamel, G., 2017. Optimization of inhomogeneous magnetization transfer (ihMT) MRI contrast for preclinical studies using dipolar relaxation time (T1D) filtering. NMR Biomed 30 (6), e3706.

Reinert, A, Morawski, M, Seeger, J, Arendt, T, Reinert, T., 2019 May 29. Iron concentrations in neurons and glial cells with estimates on ferritin concentrations. BMC Neurosci 20 (1), 25.

Rivière, D, Régis, J, Cointepas, Y, Papadopoulos-Orfanos, D, Cachia, A, Mangin, JF., 2003. A freely available Anatomist/BrainVISA package for structural morphometry of the cortical sulci. In: Proc 9th HBM Neuroimage, 192, p. 934.

Rowley, CD, Campbell, JSW, Wu, Z, Leppert, IR, Rudko, DA, Pike, GB, et al., 2021. A model-based framework for correcting inhomogeneity effects in magnetization transfer saturation and inhomogeneous magnetization transfer saturation maps. Magn Reson Med [Internet]. [citedMay 7]n/an/aAvailable from http://onlinelibrary.wiley.com/doi/abs/10.1002/mrm.28831.

Sanjeeva Reddy, T, Rajalakshmi, R, Ramakrishnan, CV, 1983 Jan 1. Lipid composition of gray and white matter in developing rat brain. Int J Dev Neurosci 1 (1), 65–74.

Schmierer, K, Scaravilli, F, Altmann, DR, Barker, GJ, Miller, DH., 2004. Magnetization transfer ratio and myelin in postmortem multiple sclerosis brain. Ann Neurol 56 (3), 407–415.

Schmierer, K, Tozer, DJ, Scaravilli, F, Altmann, DR, Barker, GJ, Tofts, PS, et al., 2007 Jul. Quantitative magnetization transfer imaging in postmortem multiple sclerosis brain. J Magn Reson Imaging 26 (1), 41–51.

Schmierer, K, Wheeler-Kingshott, CAM, Tozer, DJ, Boulby, PA, Parkes, HG, Yousry, TA, et al., 2008 Feb. Quantitative magnetic resonance of postmortem multiple sclerosis brain before and after fixation. Magn Reson Med 59 (2), 268–277.

Skripuletz, T, Lindner, M, Kotsiari, A, Garde, N, Fokuhl, J, Linsmeier, F, et al., 2008 Apr. Cortical Demyelination Is Prominent in the Murine Cuprizone Model and Is Strain-Dependent. Am J Pathol 172 (4), 1053–1061.

Skripuletz T, Gudi V, Hackstette D, Stangel M. De- and remyelination in the CNS white and grey matter induced by cuprizone: the old, the new, and the unexpected. Histopathol. 2011 Dec;26(12):1585–1597. doi:10.14670/HH-26.1585.

Song, SK, Yoshino, J, Le, TQ, Lin, SJ, Sun, SW, Cross, AH, et al., 2005 May. Demyelination increases radial diffusivity in corpus callosum of mouse brain. Neuroimage 26 (1), 132–140.

Soustelle, L, Antal, MC, Lamy, J, Rousseau, F, Armspach, JP, Sousa, PL de, 2019. Correlations of quantitative MRI metrics with myelin basic protein (MBP) staining in a murine model of demyelination. NMR Biomed 32 (9), e4116.

Soustelle, L, Antal, MC, Lamy, J, Harsan, L, Loureiro de Sousa, P., 2020 Jul 27. Determination of optimal parameters for 3D single-point macromolecular proton fraction mapping at 7T in healthy and demyelinated mouse brain. Magn Reson Med [Internet]. [cited 2020 Aug 5]Available from https://onlinelibrary.wiley.com/doi/abs/10.1002/mrm.28397.

Steelman, AJ, Thompson, JP, Li, J., 2012 Jan. Demyelination and remyelination in anatomically distinct regions of the corpus callosum following cuprizone intoxication. Neurosci Res 72 (1), 32–42.

Steiger, JH., 1980. Tests for Comparing Elements of a Correlation Matrix. Psychol Bull 87, 245–251.

Stidworthy, MF, Genoud, S, Suter, U, Mantei, N, Franklin, RJM., 2006 Apr 5. Quantifying the Early Stages of Remyelination Following Cuprizone-induced Demyelination. Brain Pathol 13 (3), 329–339.

Stikov, N, Boudreau, M, Levesque, IR, Tardif, CL, Barral, JK, Pike, GB., 2015. On the accuracy of T1 mapping: searching for common ground. Magn Reson Med 73 (2), 514–522.

Swanson, SD, Malyarenko, DI, Fabiilli, ML, Welsh, RC, Nielsen, JF, Srinivasan, A., 2017 Mar. Molecular, dynamic, and structural origin of inhomogeneous magnetization transfer in lipid membranes: origin of ihMT Contrast. Magn Reson Med 77 (3), 1318–1328.

Tagge, I, O'Connor, A, Chaudhary, P, Pollaro, J, Berlow, Y, Chalupsky, M, et al. 2016 Apr. Spatio-Temporal Patterns of Demyelination and Remyelination in the Cuprizone Mouse Model. PLOS ONE. 7;11(4):e0152480.

Thiessen, JD, Zhang, Y, Zhang, H, Wang, L, Buist, R, Bigio, MRD, et al., 2013. Quantitative MRI and ultrastructural examination of the cuprizone mouse model of demyelination. NMR Biomed 26 (11), 1562–1581.

Turati, L, Moscatelli, M, Mastropietro, A, Dowell, NG, Zucca, I, Erbetta, A, et al., 2015. In vivo quantitative magnetization transfer imaging correlates with histology during de- and remyelination in cuprizone-treated mice. NMR Biomed 28 (3), 327–337.

Underhill, HR, Rostomily, RC, Mikheev, AM, Yuan, C, Yarnykh, VL., 2011 Feb. Fast bound pool fraction imaging of the in vivo rat brain: association with myelin content and validation in the C6 glioma model. Neuroimage 54 (3), 2052–2065.

Van Obberghen, E, Mchinda, S, le Troter, A, Prevost, VH, Viout, P, Guye, M, et al., 2018 Apr. Evaluation of the Sensitivity of Inhomogeneous Magnetization Transfer (ihMT) MRI for Multiple Sclerosis. Am J Neuroradiol 39 (4), 634–641.

Varma, G, Duhamel, G, de Bazelaire, C, Alsop, DC., 2015 Feb. Magnetization transfer from inhomogeneously broadened lines: a potential marker for myelin: magnetization Transfer from Inhomogeneously Broadened Lines. Magn Reson Med 73 (2), 614–622.

Varma, G, Girard, OM, Prevost, VH, Grant, AK, Duhamel, G, Alsop, DC., 2015. Interpretation of magnetization transfer from inhomogeneously broadened lines (ihMT) in tissues as a dipolar order effect within motion restricted molecules. J Magn Reson 260, 67–76 Nov.

Varma, G, Girard, OM, Prevost, VH, Grant, AK, Duhamel, G, Alsop, DC., 2017. In vivo measurement of a new source of contrast, the dipolar relaxation time, T_{1D}, using a modified inhomogeneous magnetization transfer (ihMT) sequence: in Vivo Measurement of T_{1D} Using ihMT. Magn Reson Med 78 (4), 1362–1372 Oct.

Varma, G, Girard, OM, Mchinda, S, Prevost, VH, Grant, AK, Duhamel, G, et al., 2018 Nov. Low duty-cycle pulsed irradiation reduces magnetization transfer and increases the inhomogeneous magnetization transfer effect. J Magn Reson 296, 60–71.

Varma, G, Munsch, F, Burns, B, Duhamel, G, Girard, OM, Guidon, A, et al., 2020 Jun 30. Three-dimensional inhomogeneous magnetization transfer with rapid gradient-echo (3D ihMTRAGE) imaging. Magn Reson Med [Internet]. [cited 2020 Jul 30]Available from https://onlinelibrary.wiley.com/doi/abs/10.1002/mrm.28324.

Vega-Riquer, JM, Mendez-Victoriano, G, Morales-Luckie, RA, Gonzalez-Perez, O., 2019 Jan 7. Five Decades of Cuprizone, an Updated Model to Replicate Demyelinating Diseases. Curr Neuropharmacol 17 (2), 129–141.

Wakana, S, Caprihan, A, Panzenboeck, MM, Fallon, JH, Perry, M, Gollub, RL, et al., 2007 Jul 1. Reproducibility of quantitative tractography methods applied to cerebral white matter. Neuroimage 36 (3), 630–644.

Winkler, AM, Ridgway, GR, Webster, MA, Smith, SM, Nichols, TE., 2014 May 15. Permutation inference for the general linear model. Neuroimage 92, 381–397.

Wu, QZ, Yang, Q, Cate, HS, Kemper, D, Binder, M, Wang, HX, et al., 2008 Mar. MRI identification of the rostral-caudal pattern of pathology within the corpus callosum in the cuprizone mouse model. J Magn Reson Imaging 27 (3), 446–453.

Xie, M, Tobin, JE, Budde, MD, Chen, CI, Trinkaus, K, Cross, AH, et al., 2010 Jul. Rostrocaudal Analysis of Corpus Callosum Demyelination and Axon Damage Across Disease Stages Refines Diffusion Tensor Imaging Correlations With Pathological Features. J Neuropathol Exp Neurol 69 (7), 704–716.

Yang, HJ, Wang, H, Zhang, Y, Xiao, L, Clough, RW, Browning, R, et al., 2009 May. Region-specific susceptibilities to cuprizone-induced lesions in the mouse forebrain: implications for the pathophysiology of schizophrenia. Brain Res 1270, 121–130.

Yarnykh, VL, Kisel, AA, Khodanovich, MY., 2020 Jun. Scan–Rescan Repeatability and Impact of B_0 and B_1 Field Nonuniformity Corrections in Single-Point Whole-Brain Macromolecular Proton Fraction Mapping. J Magn Reson Imaging 51 (6), 1789–1798.
Yarnykh, VL., 2002. Pulsed Z-spectroscopic imaging of cross-relaxation parameters in tissues for human MRI: theory and clinical applications. Magn Reson Med 47 (5), 929–939.
Yarnykh, VL., 2012. Fast macromolecular proton fraction mapping from a single off-resonance magnetization transfer measurement. Magn Reson Med 68 (1), 166–178.
Zhang, L, Wen, B, Chen, T, Tian, H, Xue, H, Ren, H, et al., 2020 Jul. A comparison study of inhomogeneous magnetization transfer (ihMT) and magnetization transfer (MT) in multiple sclerosis based on whole brain acquisition at 3.0 T. Magn Reson Imaging 70, 43–49.
Zou, GY., 2007 Dec. Toward using confidence intervals to compare correlations. Psychol Methods 12 (4), 399–413.